

LATE QUATERNARY EVOLUTION OF THE MANASTASH ANTICLINE AND
MANASTASH RANGE FRONT, YAKIMA FOLD BELT, WASHINGTON:
INFLUENCE OF TECTONICS AND CLIMATE

By

Tyler Curtis Ladinsky

A Thesis Presented to

The Faculty of Humboldt State University

In Partial Fulfillment of the Requirements for the Degree

Masters of Science in Environmental Systems: Geology

Committee Membership

Dr. Harvey M. Kelsey, Committee Chair

Dr. Brian L. Sherrod, Committee Member

Dr. Lisa Ely, Committee Member

Dr. Andre K. Lehre, Committee Member

Dr. Christopher Dugaw, Graduate Coordinator

December, 2012

ABSTRACT

LATE QUATERNARY EVOLUTION OF THE MANASTASH ANTICLINE AND MANASTASH RANGE FRONT, YAKIMA FOLD BELT, WASHINGTON: INFLUENCE OF TECTONICS AND CLIMATE

Tyler Ladinsky

Evaluating the geomorphic evolution of surface processes along the Manastash Ridge and range front provided insight into the structural growth and evolution of the Manastash anticline, Yakima Fold Belt, Washington. Based on multiple independent data sets documenting episodic baselevel lowering of the Kittitas Valley relative to the Manastash Ridge range front, I infer Quaternary growth of the Manastash anticline above a south-dipping master ramp thrust. Uplift rates within the core of the anticline, calculated using luminescence dating of strath terraces, are 0.16-0.18 m/ky over the last 90 ky. Further support for Quaternary tectonic activity includes two LiDAR-identified fault scarps at the base of the Manastash range front west of the canyon entrance. Each fault scarp correlates with thrust faults evident on a seismic reflection line across the range front. Where these fault scarps occur at the base of the range front, alluvial fans are progressively truncated and uplifted by each fault scarp. Fan growth and entrenchment along the range front is driven by episodic climatic fluctuations that foster cycles of aggradation (transport-limited conditions) and incision (supply-limited conditions). I used luminescence age determinations and tephrochronology to determine that the timing of aggradation of alluvial units (Qf3, Qf2) correlates to the late

Pleistocene (MIS Stage 5) glacial-interglacial climate transition. While climate aggradation and degradation cycles control fan building events, tectonic faulting along the Manastash range front is concurrent and has elevated fans above the Kittitas Valley. Range front fault displacement of alluvial fans instigates headward retreat of stream knickpoints across multiple tributaries. Therefore, both climatic and tectonic forcing mechanisms contribute to the Quaternary landscape evolution of the southern Kittitas Valley and Manastash range front.

ACKNOWLEDGEMENTS

I owe magnitudes of gratitude for the insight, time and genuine interest exhibited by Harvey Kelsey throughout the process of this study. Without his assistance this study would have been a formless blob of data instead of the cohesive thesis presented herein. Huge thanks to Brian Sherrod for his help and knowledge during this study along with his assistance in procuring GIS data and funding of the luminescence dating. Thank you to committee members Lisa Ely and Andre Lehre for their assistance and input on my research and thesis. Thank you to Tom Pratt for the seismic reflection line data, the extensive reference collection for the Yakima Fold Belt and input on my structural interpretations. This study was supported by a NEHRP grant from the United States Geology Survey. Thank you to Elmira Wan at the USGS for providing the tephrochronologic analyses during this study. Also special thanks to Shannon Mahan at the USGS Luminescence Lab for spending the extra time and effort with our luminescence samples. Thank you to all the landowners in the Kittitas Valley and within the Yakima Canyon that allowed me land access knowingly and unknowingly. Special thanks to Rob and Louise Acheson and the Acheson Ranch for being so generous with land access. Lastly, deep appreciation and gratitude to my family and loved ones for their continued support throughout this study, including their help in the field; and all my friends and Humboldt colleagues I've met on the way!

TABLE OF CONTENTS

ABSTRACT.....	ii
ACKNOWLEDGEMENTS.....	iv
LIST OF TABLES.....	vii
LIST OF FIGURES.....	viii
LIST OF APPENDIX.....	x
INTRODUCTION.....	1
STUDY AREA.....	3
RESEARCH APPROACH.....	4
RESULTS.....	7
Pebble and Cobble Data for Tertiary and Quaternary Units.....	7
Quaternary Alluvium Units of the Manastash Range Front.....	8
Quaternary Geology of West-of-Canyon Range Front.....	10
Quaternary Geology of Yakima Canyon Entrance.....	11
Age Determinations for Quaternary Units.....	12
Incision Rates of the Yakima River and Range Front Tributaries.....	15
Range front Faulting and Fault-Related Deformation.....	16
Longitudinal Stream Profiles and Tributary Knickpoints.....	21
DISCUSSION.....	24
Baselevel Lowering Mechanisms.....	24
Glaciations of the Upper Yakima River Canyon and Northern Kittitas Valley...	25

TABLE OF CONTENTS CONTINUED

Climatic Forcing along the Manastash Range Front.....	26
Range Front Fault System.....	31
Incision Rates of Entrenched Alluvial Deposits.....	34
Comparative Incision Rates: Hanging Wall versus Footwall, Manastash Range Front Fault.....	35
CONCLUSIONS.....	37
REFERENCES.....	39
TABLES.....	42
FIGURES.....	45
APPENDICES.....	63

LIST OF TABLES

Table		Page
1	Infra-red stimulated luminescence (IRSL) K-feldspar ages Manastash anticline, Washington.....	42
2	Incision rates using uplifted strath terraces, Lower Yakima River Canyon entrance, Manastash anticline.....	43
3	Incision rates using entrenched tributary alluvial fans, west-of-the-canyon range front, Manastash Ridge.....	43
4	Incision rate calculations using fault scarps within the range front fault system, West-of-the-canyon, Manastash Ridge.....	44

LIST OF FIGURES

Figure		Page
1	Hillshade basemap of Washington and northern Oregon overlain by Quaternary faults based on the USGS fault map database.....	46
2	A 10-meter digital elevation model (DEM) of the northwestern sub-province of the Yakima Fold Belt.....	47
3	A 1m LiDAR slope map of Manastash ridge, northern range front and southwestern Kittitas Valley.....	48
4	Histograms of clast lithology and roundness from five different alluvial units.....	49
5	Regional stratigraphic column of the southwest Kittitas Valley and Quaternary lithofacies employed within the Manastash range front and lower Yakima River Canyon.....	50
6	Geologic map of the northern range front of Manastash Ridge and the southern Kittitas Valley, Central Washington.....	51
6B	Symbology and Units for the Geologic Map.....	52
7	LiDAR (1m resolution) slope map and geologic map of the west of the canyon range front, Manastash Ridge.....	53
8	Stratigraphic columns of Quaternary units within the west-of-the-canyon range front and Yakima River Canyon.....	54
9	LiDAR (1 m resolution) slope map and geologic map of the Yakima Canyon entrance, Manastash Ridge.....	55
10	Geologic cross sections.....	56
11	Migrated seismic reflection imagery.....	57
12	Annotated photograph of the Manastash range front fault system.....	58
13	Longitudinal profiles of the Manastash range front tributaries.....	59

14	Slope-drainage area plots for the range front tributaries.....	60
15	Longitudinal profile of Spring Canyon.....	61
16	Cross Section C-C'.....	62

LIST OF APPENDICES

Appendix	Page
A	Infra-red stimulated luminescence (IRSL) K-feldspar analysis by Shannon Mahan, USGS Luminescence Dating Lab, Denver CO.....64
B	USGS Tephrochronology Project Report: TL100110-1 Manastash Ridge Anticline/Yakima Fold Belt area, WA.....78

INTRODUCTION

The Yakima Fold Belt (YFB) is an extensive structural sub-province within south-central Washington primarily composed of east-west trending, north verging, narrow anticlinal ridges and broad synclinal valleys (Bentley, 1977; Reidel 1984; Figure 1). The Yakima Fold Belt covers approximately 14,000 km² and encompasses the western portion of the Columbia Plateau (Reidel et al., 1994; Tolan et al., 2009). Anticlinal ridges vary in length from 1 km to >200 km and fold wavelength from 3 to 20 km (Tolan et al., 2009; Figure 2). Typically, exposed geometry of major anticlines is asymmetrical with a steeply dipping northern limb (Tolan et al., 2009; Reidel et al., 1994). Secondary folding and faulting is common within the steep forelimb (Price et al., 1989).

Formation of the Yakima Fold Belt is the result of a north-south oriented compressional tectonic regime that was active during the middle and late Miocene (17 – 6.5 Ma) as the Columbia River Basalt poured out from the east (Reidel, 1984; Tolan et al., 2009). Based on paleo-structural measurements of variable basalt flow thickness, Reidel (1984) suggests that primary growth of the anticlines occurred during the middle to late Miocene with uplift rates of 0.25 m/ky and that these uplift rates subsequently declined to 0.04 m/ky by the end of the Miocene. However, geophysical data indicate that basement units have undergone greater amount of shortening than the overlying Columbia River Basalt Group, suggesting that folding was active prior and during the emplacement of the basalt flows (Blakely et al., 2011). Disrupted drainages, sag ponds

and grabens with cumulative vertical offset ranging from >6.5 to 9 m document Late Quaternary deformation of Saddle Mountain and Toppenish anticlines and suggest continued growth of the anticlinal ridges within the Yakima Fold Belt (Campbell et al., 1981; West et al., 1996). Reidel et al. (1994) suggests that the majority of the present structural relief has been generated after the cessation of the last major basalt (Elephant Mountain member) outpouring 10.5 Ma.

Although the age and magnetostratigraphy of the basalt is well established, deformation rates and style over the time span since deposition remain unclear. At one extreme, the anticlinal ridges that make up the Yakima Fold Belt could be topographic expressions of inactive Tertiary folds. Conversely, the folds could be constructional topographic landforms of actively growing folds that create the modern expression of the Yakima Fold Belt. Further understanding of the tectonic evolution and paleoseismic history of the Yakima Fold Belt is the impetus of this study.

In order to evaluate whether the Manastash anticline is an actively growing fold, the research has two objectives. The first objective was to document geomorphic processes along Manastash Ridge and northern range front in order to determine whether late-Quaternary-age structures or deposits have been uplifted or deformed by tectonic faulting. The second objective was to assess how climate has influenced the surficial evolution along the Manastash range front. My investigation entails geologic mapping, geochronology of Quaternary units, geomorphic/neo-tectonic mapping on LiDAR imagery, morphometric analyses of digital elevation models (DEMs), and incorporation of seismic reflection data across the range front.

STUDY AREA

My study focused on Manastash Ridge, a topographic expression of the Manastash anticline within the northwestern Yakima Fold Belt (Figures 2 and 3). The Manastash Ridge delineates the southern edge of the Kittitas Valley. Manastash anticline trends approximately N30°E to N60°E and extends 35 km as a distinct independent ridge. The eastern end of the anticline is coincident with the dying Saddle Mountain Ridge, which suggests that the Manastash anticline maybe a western continuation of the genetically linked Saddle Mountain anticline (Figure 2). Maximum topographic relief of Manastash Ridge and structural relief of the Manastash anticline are approximately 500 m and 380 m respectively (Reidel et al., 1994).

The Kittitas Valley is a northwest-elongated structural basin approximately 130 km long and 20 km wide that is occupied by the southeastern-flowing Yakima River (Figure 2). At the southern end of the Kittitas Valley, the Yakima River incises through the Manastash Ridge and enters the Lower Yakima River Canyon. Several terrace-shaped erosional remnants isolated within Kittitas Valley, such as Craig's Hill adjacent to Ellensburg and Potato Hill adjacent to the entrance to the Lower Yakima River Canyon, represent the paleo Kittitas Valley floor.

RESEARCH APPROACH

A geologic map was constructed along the Manastash range front using a suite of techniques including compilation of existing geologic maps, analysis of LiDAR imagery, inventory of alluvial clast characteristics and field mapping. Fieldwork focused primarily on mapping Quaternary surficial units. However, I collected bedding attitudes in the Tertiary basalt and sedimentary facies in order to reevaluate the structure of the Manastash anticline.

One of the primary goals of the geologic investigation was to distinguish, using an approach introduced by Waitt (1979), Yakima River (mainstream) cobble lithofacies from locally derived (sidestream) gravels. Alluvial clasts were inventoried from five different outcrops that represent distinct Quaternary lithofacies. To avoid over-sampling units with less areal extent, the sampling method was scaled to outcrop exposure. I collected 10 pebbles and/or cobbles per meter of outcrop to record lithology, diameter, roundness, and rind thickness. The minimum and maximum sample sizes were 60 and 110 respectively. Clast lithology was categorized into Columbia River Basalt Group (CRBG), Cascade Volcanics, and Other. Clast lithology and degree of clast roundness were the best criteria for distinguishing the alluvial lithofacies.

Age evaluation for the surficial units employed relative age assessment using geomorphic, geospatial, and stratigraphic relationships as well as age estimates based on microprobe tephra analyses and infrared-stimulated luminescence analyses. Microprobe analysis of a tephra sample was preformed by the United States Geological Survey

Tephrochronology Lab in Menlo Park, California. Infrared-stimulated luminescence analyses were performed on six loess and alluvial samples by the United States Geological Survey Luminescence Dating Laboratory in Denver Colorado. Relative dating assessments, tephrochronology, and infrared-stimulated luminescence analyses together provide a set of criteria for estimating ages of the Quaternary units and assessing the timing of deformation of the Manastash anticline.

I also incorporated previous age estimates for the Thorp Gravel, which is an extensive alluvial unit in the northern and western portion of the Kittitas Valley. Fission track dating methods constrain the Thorp Gravels to be 3.7 my (Pliocene) in age (Porter, 1976; Waitt, 1979). Due to lack of stratigraphic continuity and indistinct geomorphic relationships between the northern and southern Kittitas Valley, it is unclear whether the surficial units within the study area are contemporaneous with the Thorp Gravel and other units mapped by Waitt (1979). However, Bentley (1977) mapped Thorp Gravel overlying Miocene Ellensburg sediment at Potato Hill. Potato Hill is an erosional remnant in the southern Kittitas valley (Figure 3).

Acquisition of high-resolution (1 m) light detection and ranging (LiDAR) imagery for the Manastash Ridge and southern Kittitas Valley allowed documentation of Quaternary surfaces and fault lineaments along the northern Manastash range front. The LiDAR data set, collected by the Army Yakima Training Center, consists of 1 m postings projected into UTM Zone 10 NAD83 coordinate system. LiDAR survey accuracy is equivalent to 8 pulses/m².

Longitudinal profiles of Manastash range front tributaries were extracted from the 1 m LiDAR imagery. However, because Shushuskin Canyon extended beyond the boundary of the LiDAR data set, Shushuskin Canyon channel profile was extracted using 10 meter digital elevation model (DEM) imagery. Extraction of the raw data was facilitated through Matlab and ArcGIS as outlined by geomorphtools.org (Whipple et al., 2007). The raw stream gradient and drainage area data were log-transformed and the resultant slope-area plots were used to determine channel concavity (θ) of selected channels. Longitudinal profiles of tributaries were analyzed in order to document knickpoints along the range front. Compilation of knickpoint and concavity data served as a basis to delineate changes in baselevel along the range front (Kirby et al, 2001, Snyder et al., 2000, Wobus et al., 2006). The majority of tributaries within the east-of-the-canyon range front were anthropogenically influenced by highway 82, making the steep headwaters segmented from the lower reaches. To mitigate this I chose tributaries with the most continuous channel profile available.

The United States Geological Survey (USGS) provided access to a 3 km long seismic reflection line along Umtanum Road, which extends from the Kittitas Valley floor southwest into Shushuskin Canyon. The data were collected (T. Pratt, written communication, July 15, 2012) on 216 receiver channels with 5-m source and receiver spacing using a vibroseis seismic source (12-sec sweeps, 20-160 Hz frequencies). Standard CMP processing was employed. Detailed geologic mapping within the vicinity of the seismic reflection line enabled a composite structural interpretation of the geometry of the Manastash range front and fault system.

RESULTS

Pebble and Cobble Data for Tertiary and Quaternary Units

Histograms of pebble lithology and pebble roundness from five different localities, four Quaternary units and a Miocene Ellensburg conglomerate, document the composition of the surficial units (Figures 4 and 7). Modern Yakima River and paleo-Yakima River deposits had significantly different percentages of Columbia River Basalt Group clasts with modern alluvium having 44% CRBG and the paleo-Yakima River alluvium having 75% CRBG clasts (Figure 4). Degree of roundness further differentiated modern and paleo-Yakima River alluvium. The modern Yakima facies has predominately rounded (35%) and sub-rounded (32%) pebbles while the paleo-Yakima facies were predominately sub-rounded (33%) and sub-angular (29%).

Both Spring Canyon and Shushuskin Canyon fan deposits yield identical lithologic compositions of 100% CRBG. Dominant pebble roundness varied slightly between angular and sub-angular for both localities with respective values of 44% and 33% for Spring Canyon and 36% and 43% for Shushuskin Canyon.

Pebble lithology and pebble roundness for the Miocene Ellensburg conglomerate facies are distinct from the Quaternary facies (Figure 4). For the Miocene conglomerate, the dominant clast is a rounded (43%) Cascade volcanic clast (62%).

Quaternary Alluvium Units of the Manastash Range Front

Geologic mapping focused on identifying surficial units that document the transition from the topographic highland to the Yakima River floodplain at the south end of the Kittitas Valley. The Quaternary units consist of alluvial deposits of the Yakima River watershed that include detritus sourced in the Cascade Range and tributary alluvial deposits whose source is the Columbia River Basalt Group (CRBG) of the Manastash Ridge (Figure 5). Yakima River alluvial deposits include both modern alluvium and terrace deposits that are now elevated above the Yakima River floodplain.

The tributary alluvium accumulated as fan deposits along the range front or within the lower reaches of tributaries that debouch onto the floodplain of the Yakima River. I separated the alluvial fan deposits into seven units of increasing relative age based on elevation and degree of preservation of fan morphology (Figure 5). Loess deposits of varying thickness and degrees of cementation cap fan surfaces. Loess deposits were noted in the field but not differentiated by relative age (Figure 5). Mapping loess by relative thickness and soil development was beyond the scope of this investigation, and capping loess units were included in the fan units that the loess overlies. However, loess deposits were the target sample material for infrared stimulated luminescence analysis, and the relative age for these specific loess deposits was determined through field work and LiDAR terrain analysis.

The range front tributary alluvial fan deposits have distinctly different geomorphic characteristics to the west and east of the entrance to the Lower Yakima River Canyon (Figure 3). Therefore, the ensuing description contrasts the west-of-the-

canyon and east-of-the-canyon range front. Along the range front east of the canyon entrance, the tributary alluvial fans are thin (1 – 3 m), expansive, dissected and extend up to 2.5 km onto the Kittitas Valley floor. Five generations of increasingly higher and older fans are mapped based on geomorphic preservation and morphostratigraphic position (Figure 6). Field exposures indicate fan surfaces east of the canyon entrance were deposited unconformably onto the Upper Ellensburg Formation (Tue), the unconformity representing the paleo-pediment that bounds the southern margin of Kittitas Valley. Successively younger fans originate at the mouth of older entrenched fan deposits and extend further northward onto the valley floor. Younger fans also are nested and inset within older fan systems (Figure 6). Both the scarcity of Yakima River lithofacies within the distal edge of the terraced fan deposits adjacent to the valley floor combined with extensive Quaternary fan progradation of the locally derived sidestream gravel indicate that the Yakima River has not migrated to the east of the canyon entrance during the late Quaternary.

In contrast, in the west-of-the-canyon range front, tributary alluvial fan deposits are small, the fans are steeper, and the fans are confined within tributary canyons incised into the basalt of the range front. Only the youngest fans extend beyond the tributary mouth onto the Kittitas Valley floor. Based on elevation and geomorphic position along the range front west of the canyon entrance, there are four generations of fan surfaces (Figure 7). Fans are constructed by debris flows that are generated in the steep tributary headwaters and then deposited in the lower reaches within the tributary canyon or on the

valley floor of the Yakima River floodplain. Subsequently the distal edges of the alluvial fans are eroded by the Yakima River.

Quaternary Geology of West-of-Canyon Range Front

West of the Yakima River canyon entrance, LiDAR imagery and field mapping yield abundant evidence for active and entrenched alluvial fans within multiple tributary canyons incised into the range front (Figure 7). Spring Canyon (Figure 3) provides the most complete record with four distinct sidestream alluvial fan deposits representing former elevations of the Spring Canyon tributary channel (Figure 7 and 15). The youngest Quaternary fan deposit (Qf1) slopes gently between 5° and 10° onto the valley floor. The next-youngest Quaternary fan deposit (Qf2) is well preserved and has the largest areal extent (Figure 7). Unit Qf2 is generally 2-3 meters above active tributary channels and has slopes ranging between 3° and 10°. Quaternary fan deposit three (Qf3) is best preserved at Spring and Benwy Canyons (Figure 7) and consists of a series of relatively flat-lying terraces approximately 10 meters above the active channel. The oldest and most distinct alluvial unit along the west-of-canyon range front, Quaternary fan deposit four (Qf4), is approximately 18 meters above the active tributary channel at Spring Canyon. Unit Qf4 ranged in slope from 5° to 20°.

A composite alluvial fan stratigraphic section of Qf4 at the north distal flank of Spring Canyon (Figure 8A) indicates multiple deposits of sidestream alluvium interbedded with loess units of varying thickness. The thickness of alluvial and loess packages vary with distance from the tributary mouth. Generally, deposits proximal to

the tributary channel mouths have thicker packages of alluvium while exposures distal to the tributary have thicker deposits of loess (e.g., Figure 8A).

Lateral erosion by the Yakima River is greater in areas closer to the lower Yakima River Canyon entrance. Because such lateral erosion trims the range front and accelerates downcutting of tributaries flowing perpendicular to the range front, the relatively older fan deposits are less well preserved in tributaries closest to the canyon entrance.

Situated at the flanks of Long Tom and Shushuskin canyons are paleo-Yakima River gravels (Qg5) 70 m to 82 m above the valley floor (Figure 7). The presence of the Cascade-derived lithology in the terrace gravels implies the Yakima River abutted against the paleo-Manastash range front in Qg5 time. Although unit Qg5 is likely younger than the Thorp Gravel (Waitt, 1979), both the mainstream Thorp Gravel and Qg5 gravel have a Cascade Range source.

Quaternary Geology of Yakima Canyon Entrance

A series of strath terraces occur in the Yakima River Canyon two kilometers south of the canyon entrance (Figure 9). The Yakima Canyon terraces are located on the northern and southern edge of an abandoned meander (Figure 9A) and illuminate the history of incision through the Manastash Ridge by the Yakima River. The elevationally higher northern terraces, 40 to 135 m above the meander loop, document the initial creation and subsequent incision of the meander. Paleo-Yakima River gravels (units Qg6, Qg5, and Qg4) exposed within the tributary canyons and southern flanks of the terraces are unconformably deposited on Columbia River Basalt. These paleo-Yakima

River gravel units are in turn overlain by tributary fan alluvium (units Qf5, Qf4) (Qg4 overlain by Qf4, Figure 8B). The distinct contrast of mainstream river gravels (Qg5, Qg4) overlain by sidestream lithofacies (Qf5, Qf4, Qf3) within the terrace sequence suggests abandonment by the Yakima River was followed by fan building.

In contrast, the southern terrace sequence (Qg2 overlain by Ql2), south of the abandoned meander loop, is younger and lower in elevation than units Qg5 and Qg4 and documents incision post-abandonment of the meander loop (Figure 8B). Terrace exposures record a bedrock strath surface cut on Columbia River basalt 19-20 m above the Yakima River channel. The strath is overlain by a 6 to 7 m thick paleo-Yakima River gravel package (Qg2), which is in turn overlain by a 3 m thick clean loess (Ql2) (Figure 8C).

Age Determinations for Quaternary Units

Infrared stimulated luminescence (IRSL) age determinations were performed by Shannon Mahan at the USGS Luminescence Dating Lab, Denver, CO on silt and fine sand samples from fan and terrace deposits west of the canyon mouth and within the canyon (Table 1). Quartz optically-stimulated luminescence (OSL) was initially planned, but because of a slow decay signal retrieved from the samples during luminescence, quartz OSL was abandoned. An alternative approach involves luminescence of K-feldspars using infrared diodes referred to as Infrared-Stimulated Luminescence (IRSL). For younger samples (< 100 ky), IRSL dating works well, while for older samples (> 100 ky), IRSL ages are too young. The erroneously young ages are a function of “anomalous

fading” of K-feldspars (Morthekai et al., 2011). Anomalous fading is an observation in which electrons “tunnel” from principal luminescence traps to nearby structural defects in sediment. Anomalous fading of the feldspars from infrared-stimulated luminescence analyses produced an underestimate of ages for several samples (MN10-1, MN10-3, MN10-4, and AM10-2, Appendix A). The determined fade rates for samples MN10-1, MN10-3, MN10-4 were 11% to 18%, while sample AM10-2 produced a fade rate of 8% (Appendix A). An average fade rate of all the samples was calculated to be 12%, which is similar to a anomalous fade rate correction (13%) used by Morthekai et al.(2011). Therefore a fade correction rate of 13% was used to determine minimum ages of the samples (Table 1, Appendix A). Three loess exposures intercalated within Qf4 sidestream alluvial deposits along the west-of-the-canyon range front produced IRSL minimum ages ranging between $215,880 \pm 10,310$ and $279,020 \pm 31,240$ (Table 1).

Analysis of a loess (MN10-5) capping Qf3 in the west-of-canyon range front area indicated an IRSL age of $20,860 \pm 1,520$ (Table 1, Figure 7). Based on the large difference between IRSL ages of Qf3 (20.9 ka) and Qf4 (>280 ka) and between the tephrochronologic age for Qf3 (100 ka) versus the IRSL age for loess capping Qf3 (20.9 ka), I conclude that the loess cap of Qf3 (sample MN10-5) represents deposition that is substantially younger than the underlying alluvial deposit Qf3. Therefore the IRSL sample MN 10-5 does not inform the age of Qf3. The alternative 100 ka age for Qf3, discussed below, comes from tephrochronology.

Infrared stimulated luminescence (IRSL) analyses were also performed for the mainstream paleo-Yakima River alluvial deposits or overlying loess situated within or

adjacent to the abandoned meander loop near the lower Yakima River Canyon entrance (Figure 9). IRSL samples were acquired from the northern (Qg4) and southern (Ql2) strath terrace sequences (samples AM10-2 and AM10-1 respectively). The Qg4 terrace sediment produced a minimum age of $254,250 \pm 17,080$ and the Ql2 loess cover above Qg2 terrace gravel produced an age of $88,750 \pm 4,520$ (Table 1). Therefore infrared stimulated luminescence analyses indicate the Yakima River was actively incising within the meander at 250 ka and the Yakima River had abandoned the meander loop by 90 ka.

Tephra sample TL100110-1 was collected at the distal edge of fan deposits Qf3 adjacent to the mouth of Spring Canyon (Figure 7). The 5 cm thick discontinuous tephra unit intercalated with fan alluvium, appeared to be reworked airfall tephra. Based on microprobe investigation of glass in the tephra, the glass correlates well (0.976 and 0.96) to the 100 ka Carp Lake (CL-90A or CARP-10) tephra sequence (Carp Ash-10 of Whitlock et al., 2000; E. Wan, written communication, March 31, 2011, Appendix B). The Carp Lake tephra (Carp Lake ash-10) is not dated directly but rather is extrapolated from an age-depth regression model from a core of Carp Lake, which yielded ages between 90 ka and 125 ka (Berger et al., 1995; Whitlock et al., 2000). The younger age bounding the regression model was determined by thermoluminescence methods (Berger and Busacca, 1995), and the older age bound was determined from deeper (older) tephra with distinctive glass geochemistry. Therefore, the 100 ka Carp Lake tephra is an estimated age. Given that Whitlock et al., (2000) assigned two additional tephra ages of 218 and 190 ka which were only 2 m lower in the core than the 100 ka tephra, it is

possible that the 100 ka Carp Lake tephra could actually be tens of thousands of years older (Whitlock et al., 2000).

Incision Rates of the Yakima River and Range Front Tributaries

In order to quantify incision within the study area, I calculated five incision rates using IRSL and tephrochronology age constraints. Two incision rates were determined for the mainstream Yakima River alluvial deposits from the southern and northern terrace sequence within the Yakima Canyon entrance (Figure 9; Table 2). The southern strath terrace stratigraphic sequence (sample AM10-1) yields an incision rate of 0.16m/ky to 0.18m/ky. However, the IRSL age constrains the age of the capping loess (Q12) and the strath surface is 9 m below the sample site in the loess (Figure 8C). The actual timing of incision into the strath surface would be older, by the amount of time required to deposit 2 m of loess, assuming that the gravel is coeval with the age of strath formation. Therefore the incision rate 0.16m/ky to 0.18m/ky is maximum limiting and the actual incision rate may be less.

Fluvial terrace deposit Qg4 from the northern strath terrace sequence (sample AM10-2) yielded incision rates of 0.18 to 0.2 m/1000 yrs (Figure 8B; Table 2). However, ages used to calculate incision rates were based on fade-corrected IRSL age determinations that represent minimum ages and therefore constrain only the maximum incision rate. The minimum incision rate (Table 2) represents the lower bound of the maximum incision rate for paleo-Yakima River deposits (Qg4).

Three incision rates were also calculated from sidestream entrenched tributary alluvial fan deposits along the west-of-the-canyon range front (Table 3). Total incision was calculated from top of the entrenched fan surface to current tributary thalweg. Long Tom Canyon yields an incision rate of 0.02 to 0.03 m/ky (Table 3), while Spring Canyon yields an incision rate between 0.06 and 0.09 m/ky. Since the incision rates for Long Tom and Spring Canyon were based on fade-corrected IRSL analyses, which represent minimum ages, the incision rates (Table 3) constrain only the upper limits of the incision rates. Using tephrochronology analysis and stratigraphic interpretation from a distal fan deposit (Qf3) at the mouth of Spring Canyon (Figure 9), I considered the age of Qf2 at the mouth of Dead Cow Gulch south (Figure 7) to be less than 100 ka and a corresponding minimum incision rate to be 0.08 m/ky (Table 3).

Range Front Faulting and Fault-Related Deformation

The principal structures of Manastash Ridge are the large, open asymmetrical Manastash anticline and associated range front fault system (Figures 6 and 10). The forelimb of the Manastash anticline is composed of two small subsidiary structures, the Manastash syncline and Thrall anticline (Bentley, 1977) (Figure 10). Northeast-vergent range front thrust faults daylight along strike to the northwest; to the southeast, a range front thrust fault does not daylight but a backthrust is evident in the forelimb of the Manastash anticline (Figure 6).

Two approaches were employed to investigate range front and fault-related deformation. The first approach was Quaternary geologic mapping of the range front in

conjunction with analysis of LiDAR imagery. The second approach was to investigate deformation in cross section at two transects perpendicular to the range front where structure is revealed across strike. One of the transects is along the Yakima River canyon where roadcut exposures and natural exposures in the steep canyon walls provide insight to deformation and faulting. The other transect is along Shushuskin Canyon, which is incised into the range front. Although the road along the canyon bottom provides some exposures that reveal bedrock structure, the main source of structure and fault data along Shushuskin Canyon is a seismic reflection line shot along the road alignment.

The Manastash range front fault system trends along the base of the range front west of the canyon entrance. As identified using LiDAR, seismic imagery and field mapping (Figures 6, 7, and 11), the range front fault system west of the canyon entrance consists of two distinct thrusts fault systems ('northern fault system' and 'southern fault system').

The northern fault system, trending N40°W north of Shushuskin Canyon and N60°W south of Shushuskin Canyon, delineates the transition from the gently sloping valley floor and Yakima River floodplain to the moderately sloping alluvial deposits at the north margin of the range front. The northern trace of the range front fault system, mappable only west of the canyon entrance, trends approximately N40°W along Shushuskin and Long Tom Canyons where it juxtaposes the older upthrown alluvial unit Qf4 with younger and lower alluvial unit Qf2 (Figure 7). This fault is also seen on the seismic reflection line trending along Shushuskin Canyon. The seismic imagery depicts the fault scarp, 6 to 9 m high, daylighting at station 470 (Figure 11). The highly

reflective, shallow and sub-horizontal alluvial sediments on the northeast side of the inferred fault are thrust under brecciated basalt units that bound the southwest side of the northern range front fault (Figure 7B and 11). The alluvium-basalt contact is defined by the strong reflection between depths of 350 to 400 meters in the footwall of the northern range front fault. The 350-400 m depth of the contact indicates the minimum vertical offset of the range front fault system (Figure 11).

Further southeast along the range front, the northern fault system splays at Dead Cow Gulch North into two distinct fault scarps (Figure 7). The lower and younger fault scarp, 6 to 10 m high, juxtaposes alluvial units Qf1 and Qf2 (Figure 7 and 12). Based on the steepness of the lower scarp face, I infer that the lower scarp may be Holocene in age. A small exposure of both Columbia River basalt (Tw) and Ellensburg Formation (Teu) outcrops on the upthrown (southern) side of this fault and documents uplift along the hanging wall (Figure 7 and 12). The upper and older fault scarp, which is 10 to 12 m high at Dead Cow Gulch South and trends N55°W, is similar to the fault scarp expressed at Long Tom Canyon where it juxtaposes units Qf4 and Qf2 (Figures 7 and 12).

Moving even further southeast from Dead Cow Gulch South, the surface trace of the northern fault system moves out onto the valley floor and any evidence of recent faulting has been removed by Yakima River erosion. Elevated and abandoned alluvial deposits within Spring Canyon and at the mouth of Benwy Canyon are consistent with the presence of the northern range front fault extending out onto the valley floor west of the canyon entrance (Figure 7).

The southern range front fault system traces the paleo range front-valley floor junction that follows the southwestern contact of unit Qf4 (Figure 7). Adjacent to Shushuskin and Long Tom Canyons, the southern range front fault scarp, approximately 10 m to 25 m high, juxtaposes paleo-Yakima River deposit Qg5 to the southwest and unit Qf4 to the northeast (Figure 7). Where the scarp crosses the seismic line, the seismic line shows a fault daylighting at the surface (Figure 6; Figure 11). South of Shushuskin Canyon the southern range front fault system juxtaposes basalt to the southwest against alluvial unit Qf4 to the northwest. Based on subsurface seismic imagery (Figure 11), I infer that the southern range front fault system daylights at station 260 and truncates both a syncline in the hanging wall and an anticline in the footwall. Therefore, the anticline-syncline sequence that is better exposed along the Yakima Canyon road is also evident at Shushuskin Canyon where the syncline-anticline sequence has been thrust over itself along southern range front fault (Figure 11).

I infer that the distinct topographic break in slope, evident along the range front between Long Tom Canyon to the northwest and Shushuskin Canyon to the southeast (Figure 7A) and traced by the contact between basalt and alluvial unit Qg5 (Figure 7B), is due to fluvial incision as the Yakima River abutted against the basalt range front. The presence of paleo-Yakima River deposits Qg5 is consistent with incision and trimming of the range front by the Yakima River followed by uplift and isolation of the alluvial deposits Qg5 and Qf4 due to slip from the southern range front fault system.

The other fault that is associated with the Manastash range front fault system is a backthrust; this backthrust is the only surface expression of faulting within, and east of,

the canyon entrance. Deformation 0.6-1.2 km south of the Manastash range front is well exposed in road cuts in the Yakima River canyon south of the canyon entrance. Bentley (1977) discusses deformation inferred from these exposures. Stratigraphy of individually identified basalt and interbasalt units evident in the canyon road exposures (Bentley, 1977), in conjunction with bedding attitudes, documents the folded structure of the Manastash anticline forelimb (Figure 10A). I supplemented Bentley's (1977) lithologic mapping with strike and dip measurements along the road cuts and infer that a steeply dipping backthrust intersects the Manastash Syncline axis to accommodate the truncation of the Squaw Creek Member (Tesc) in the northern limb. The disappearance of the Squaw Creek Member on the northern limb is a consequence of uplift and erosion of the hanging wall of the backthrust (Figure 10A). Based on the structural trend of bedrock exposures 0.75 km south of the canyon entrance, I infer that the steeply dipping backthrust trends N60°W. Striations and slickenlines noted within the Manastash syncline yield a predominant trend sub-perpendicular to the fold axis suggesting shearing was primarily due to flexure as tightening of the syncline advanced. Trend and plunge observations indicate primary dip-slip motion because striation and slickenline rakes range from 41° to 65°.

In summary, a combination of field mapping with fault geometry determined from seismic imagery indicates the range front fault system west of the canyon entrance consists of two reverse faults that dip approximately 30° south under Manastash Ridge (Figures 7 and 11). These two reverse faults do not extend as subaerially discernable traces eastward into the canyon entrance area. Rather, a backthrust in the deformed

forelimb of the Manastash anticline characterizes the faulting in the canyon entrance area. Based on road cut exposures at Vanderbilt Gap 5.2 km to the east-southeast, the Washington Department of Natural Resources (1994) maps a steeply dipping backthrust truncating the southern limb of a syncline. Therefore, from the geologic mapping at Vanderbilt Gap, I infer that the backthrust evident in the Yakima River canyon exposures continues eastward along strike to Vanderbilt Gap.

Longitudinal Stream Profiles and Tributary Knickpoints

Eight tributaries (Northeast 1, Northeast 6, Noname Canyon, Benwy Canyon, Spring Canyon, Dead Cow South, Dead Cow North and Shushuskin Canyon; Figure 3) were chosen to investigate channel longitudinal profiles across the range front and determine respective channel concavity (θ). Because rate of fluvial incision responds to the rate of baselevel fall, a graded river profile demonstrates fluvial equilibrium (Zaprowski et al., 2005). Bedrock rivers, because of the inability of bedrock channels to quickly adjust to external perturbations, tend to retain evidence of disequilibrium due to tectonic, climatic, and/or eustatic driving mechanisms. Knickpoints within the longitudinal profile, and concavity (θ) values, can provide a proxy for areas along the range front where the fluvial systems are in disequilibrium due to climatic and/or tectonic influences (Snyder et al., 2000; Kirby et al, 2001; Wobus et al., 2006).

Two tributaries, Northeast 1 and Northeast 6, were used for east-of-the-canyon range front profile and knickpoint assessment. Based on the lack of evidence of range front faulting, I infer the tributary channels should not be perturbed by baselevel fall.

Concavity (θ) values of channels within east-of-the-canyon range front fall between 0.44 and 0.60. These values are consistent with a profile that has a moderately steep concave headwater profile followed by a gentle, smooth sloping profile grading to the valley floor (Figures 13 and 14). Lack of knickpoints within the longitudinal profiles suggests minimal fluctuation in baselevel.

In contrast, six tributaries were analyzed from west-of-the-canyon range front that flow perpendicular to the range front fault system. These tributaries demonstrated irregular headwater profiles followed by steeply sloping channel geometries with concavity (θ) values that range between 0.11 to 0.48 (Figures 13 and 14).

Noname, Benwy and Spring canyons all exhibit a knickpoint along the lower reach of their respective channel profile at a correlative elevation of approximately 510 meters (Figure 13B). Knickpoints responding to the same baselevel change tend to be found at constant elevation among tributaries systems of different drainage area because knickpoints migrate through fluvial systems at a rate proportional to tributary drainage area (Wobus et al., 2006). A coincident knickpoint indicates a common baselevel lowering event that is simultaneously translating through the adjacent tributaries (Noname, Benwy Spring Canyon, Figure 13) as a wave of incision.

To understand how knickpoints relate to the entrenched alluvial fans, I superimposed the entrenched alluvial fan surface elevations onto the longitudinal profile of Spring Canyon (Figure 15). Point elevations from each alluvial unit (Qf2, Qf3, Qf4) were projected horizontally onto the vertical plane containing the channel thalweg thereby defining fan surface elevations above the tributary thalweg. If I project a relict

channel profile of Spring Canyon downstream from the knickpoint at 510 m, such a relict profile would intersect the surface elevations of alluvial fan unit Qf4 (Figure 15B). This suggests that the knickpoint at 510 m elevation records the present position of the knickpoint that started to retreat headward upon initiation of baselevel fall at the time of abandonment of Qf4 as the active depositional surface (Figure 15). By inference, the presence of each successively lower entrenched alluvial unit indicates a separate baselevel lowering accommodated by incremental lowering of the Kittitas Valley floor relative to the mouth of Spring Canyon.

DISCUSSION

Baselevel Lowering Mechanisms

On the basis of tributary longitudinal profiles, entrenched alluvial deposits and fault scarps at range front positions, I infer periodic episodes of baselevel fall within the tributaries draining northward off the Manastash range front onto the Yakima River flood plain. Two possible mechanisms driving episodic baselevel fall are 1) tectonic uplift of Manastash Ridge or 2) erosional degradation of the Yakima River floodplain and the Kittitas Valley. A tectonically driven model would predict uplift of the range front with concurrent genesis of fault scarps while a climatic model would require progradation of alluvial fans associated with aggradation of the Kittitas Valley followed by fan incision and erosion by the Yakima River. Conceptually, either mechanism can produce entrenched alluvial fans, erosional or fault scarps, and induce a migrating knickpoint response within tributary systems (Schumm, 1993, Ritter et al., 1995).

A tectonic model is consistent with the regional tectonic context of the Yakima Fold Belt (Price et al., 1989; Riedel et al., 1993), where I infer the steeply dipping Manastash forelimb is folded and uplifted by a north verging thrust fault that daylights within the Manastash range front. Periodic uplift along the hanging wall of a south dipping thrust fault would accommodate growth of the Manastash anticline, generate range front fault scarps, and lower the valley floor baselevel.

Alternatively, a competing driving mechanism of baselevel lowering would be erosional degradation of the Kittitas Valley by the Yakima River due to late Quaternary

climate fluctuations. A climatic model suggests that late Quaternary glacial interglacial periods would foster cycles of aggradation (transport-limited conditions) and incision (supply-limited conditions) (Porter, 1976; Waitt, 1979).

Glaciations of the Upper Yakima River Canyon and Northern Kittitas Valley

Porter's (1976) mapping of six distinct Pleistocene glacial outwash terraces documents alpine glacier advances into the northern Kittitas Valley and subsequent aggradation. Sequences of outwash terraces, 5 to 140 m above the active Yakima River channel, indicate periods of sedimentation followed by fluvial degradation and incision. Porter (1976) used pedogenic and weathering rind analyses to divide the alpine glacial sequence in the northern Yakima River Canyon into two major glacial advances, the Kittitas Drift and the Lakedale Drift. The Kittitas Drift corresponds to the penultimate glacial advance (marine isotope stage 6), which peaked between 130 to 140 ky, and is composed of two glacial phases, the Swauk Prairie member and Indian John member (Porter, 1976; Waitt, 1979). Outwash terraces adjacent to terminal moraines from the Kittitas Drift are situated 100 m above the Yakima River and expose extensive fluvial boulder-cobble gravel units intercalated with finer gravel and sand units (Porter, 1976). The Lakedale Drift is composed of several outwash terraces, 5 to 10 m above the Yakima River channel, and correlates to the Frasier Glaciation of the Puget lowland that reached maximum extent 14,000 yr ago (Waitt, 1979).

In summary, the Yakima River and Kittitas Valley have experienced dramatic shifts in sediment yield and transport capacity due to late Quaternary climate fluctuations.

Furthermore, a terminal moraine impounded sediment and meltwater during retreat of the Indian John glacial phase creating a lake 275 m deep, 15 km long and 3 to 5 km wide. When breached, the lake must have caused massive aggradation and erosion in the Kittitas Valley (Porter, 1976).

Climatic Forcing along the Manastash Range Front

While tectonics generates relief suited for fan building, fan building and entrenchment within active tectonic environments have been principally related to climate (Ritter et al., 1995; Spelz et al., 2008). A climate controlled alluvial fan model for arid environments proposed by Bull (1991) relates periods of fan building to transition from glacial to interglacial cycles where warming conditions and low soil moisture and vegetation cover cause increased sediment production. Aggradation continues until a geomorphic threshold is crossed wherein the hillslope sediment reservoir is depleted causing the fluvial system to become supply limited, which initiates incision and entrenchment (Bull, 1991; Spelz et al., 2008). An alternative model for fan building (Harvey et al., 1999) suggests that inset alluvial fan sequences relate to wetter conditions associated with glacial periods. Fan building would be synchronous with outwash events. As the climate conditions altered to interglacial periods, incision and entrenchment would dominate the geomorphic system (Harvey et al., 1999). Regardless, a diagnostic attribute for climate forcing is synchronous aggradation followed by synchronous incision within a region (Ritter et al., 1995).

While Porter (1976) and Waitt (1979) document glaciation and subsequent aggradation in the Upper Yakima River Valley and the northern Kittitas Valley, it is unclear whether the Manastash range front and Lower Yakima River Canyon were similarly affected by aggradation during glacial periods. However, ages of alluvial deposits along the Manastash range front can constrain timing of fan aggradation. IRSL analysis of a capping loess deposit (Ql2) within the canyon entrance indicates the loess was deposited at about 90 ka suggesting aggradation of underlying Qg2 is thus slightly older than 90 ka (Table 1). Based on tephrochronology I infer that Qf3 was actively prograding at 100 ka and perhaps tens of thousands years prior to or after 100 ka. Therefore aggradational timing of Qf3 and Qf2 appears to be post-Kittitas Glaciation (130-140 ka) and well before Lakedale glaciation (14 ka). Given the age estimates above, I infer that aggradation of Qf3 and Qf2 is associated with the marine oxygen isotope stage 5 (MIS 5) interglacial. The MIS 5 interglacial, from approximately 130 ka to 100 ka, was the period directly following the Kittitas Glaciation. Aggradation during the interglacial dryer and warmer conditions indicates the preferred fan-building model is consistent with the arid model proposed by Bull (1991). IRSL analyses for Qf4 consistently yielded a minimum age of 250 ky (Table 1), which suggests aggradation of Qf4 predates the Kittitas and Lakedale glaciations. A minimum age constraint does not permit correlating aggradation of Qf4 to a specific glacial and interglacial cycle. However, geomorphic mapping of fan deposits along the entire range front suggests a cyclic pattern including up to three periods of fan building older than Qf4 (Figure 6). Furthermore, the apparent similarity in areal extent, elevation, IRSL and

tephrochronology ages between alluvial deposits situated along the range front and Yakima River Canyon indicates syndepositional fan aggradation driven by optimal climatic conditions.

Alluvial fans along the west-of-canyon range front are distinctly separated by scarps ranging in height from 6 to 12 m high (Figure 7). If climate is the driver of fan aggradation episodes, what process is accountable for the distinct separation of fans by scarps? While it is plausible for the two sets of scarps to be generated exclusively by climatically-driven cycles of deposition and erosion, I infer that, based on the different elevations between the two sets of scarps, the conspicuous alignment evident within each scarp set, and that the two scarp sets juxtapose alluvial units of different ages (Figure 7), that these are fault scarps not erosional features.

The preservation of an erosional scarp along the range front that truncates the distal edge of fans requires, first, fan progradation onto the Kittitas Valley floor, and, second, migration of the Yakima River laterally southwestward thereby eroding the distal edges of the alluvial fans and creating an erosional escarpment. Assuming that progradation of alluvial fans off the range front is synchronous with aggradation of the valley floor, Qf2 documents tributary-fan progradation as the Yakima River was aggrading. As the climatic conditions initiated entrenchment and incision by the Yakima River, concurrent with southwest migration towards the range front, an erosional scarp would be developed as exhibited by the lower scarp delineating Qf2 and Qf1 at Dead Cow Gulch South (Figure 7). The higher elevational scarp between Qf4 and Qf2 that extends from Long Tom Canyon southeastward across Shushuskin Canyon to Dead Cow

Gulch South (Figures 7A and 12) could be explained with the same mechanism, but during a previous aggradation and degradation cycle. However, for the older scarp to be higher and elevationally separated from the lower Dead Cow Gulch South scarp would require erosion of the Kittitas Valley and associated prograded fans by approximately 24-36 m between the upper older fan-building and lower younger fan-building events.

Other criteria for evaluating the role of climate forcing in generating baselevel fall along the Manastash range front are tributary longitudinal profiles and profile concavity (θ) values from east-of-the-canyon versus west-of-the-canyon range front tributaries. Based on the difference in channel geometry, knickpoints, and concavity (θ) values in east-of-canyon tributaries versus west-of-canyon tributaries, I infer the two fluvial settings are differentially influenced by tectonic forcing (Kirby et al, 2003). Irregularities in channel geometry that can be attributed to tectonically induced baselevel fall are only found within the west-of-the-canyon range front tributary system where the range front fault system is identified. Conversely, a climate signal is most prominent within east-of-the-canyon fluvial system where there is no evidence for tectonic forcing. By so distinguishing between the two fluvial systems, I can decouple the climatic and tectonic signals.

High concavity values, as noted within east-of-the-range front tributaries ($\theta = 0.44$ and 0.60), suggest that uplift rates decrease in the downstream direction (Kirby et al., 2001). Geologic mapping (Figure 6) shows that tectonic uplift is concentrated in the ridgeline south of the fluvial system and the range front to the north exhibits no surficial evidence of active faults. Furthermore, cyclic entrenchment of older alluvial fans

followed by deposition of younger fans prograding outward onto the valley floor ultimately producing a large, broad, nested alluvial fan is indicative of a climate signal (Ritter et al., 1993, Spelz et al., 2008, Bull 1992). Inset fans document that incremental fan growth basinward was accommodated by entrenchment and dissection of older fan units by the steep, small, ephemeral tributaries flowing northward onto the valley floor. Lack of any channel knickpoints within the eastern fluvial systems (Figure 13) suggest profile equilibrium, where the rate of incision is balanced with baselevel lowering. These small ephemeral tributaries with weak erosive ability, demonstrating channel profile equilibrium, suggest a low magnitude baselevel lowering signal that is congruent with a fluvial system driven by gradual climatic conditions.

West-of-the-canyon range front fluvial systems, in contrast, demonstrated a wide variation in concavity values (0.11 to 0.48). The complex longitudinal profile geometry of Spring Canyon made determining the concavity difficult to assess (Figure 15). The large convexity within the headwater of Spring Canyon, attributed to colluvial-dominated processes, pushed the upper limit for determining the concavity to be extended downstream of the prominent convexity (Figures 14 and 15). Concavity values calculated for tributaries Noname, Benwy and Shushuskin exhibited low values ranging between 0.11 to 0.38 (Figure 14). Low concavity values in tectonically active areas have been noted in fluvial systems where the uplift rate increases downstream (Kirby et al., 2001). I infer that uplift rate increases downstream within the west-of-the-canyon range front tributaries as a consequence south-side-up displacement on the range front fault system. In addition a elevationally coincident knickpoint, noted between Noname,

Benwy, and Spring Canyon tributaries, suggests the fluvial systems are responding to a synchronous baselevel fall among these tributaries (Wobus et al., 2006). Documentation of disequilibrium through coincident knickpoints and low concavity values along the west-of-the-canyon fluvial system, in contrast to the apparent equilibrium within the east-of-the-canyon tributaries, is consistent with our suggestion that tectonic motion dominates range front landscape evolution west of the canyon entrance.

In order to calculate a climate related longterm incision rate of the Kittitas Valley relative to the Manastash range front, a cross section was constructed connecting the range front east of the canyon to Potato Hill (Figures 6 and 16). Field and geomorphic mapping identified upper Ellensburg Formation exposures underlying the alluvial fan deposits east-of-the-canyon range front, which depicts paleo-range front elevations that can be interpolated to connect to the erosional remnant of Potato Hill (Figures 16). Using the Thorp Gravel (3.7 My, Waitt, 1979) capping Potato Hill as an age constraint, an average erosional lowering rate for the southern Kittitas Valley during the last 3.7 Ma is 0.007 to 0.01 m/ky.

Range Front Fault System

Distinct fault scarp lineaments, at the mouth of Long Tom Canyon and at the mouth of Dead Cow Gulch South, collectively delineate the northern range front fault system (Figures 7 and 12). Based on the scarp facing direction and exposed Columbia River Basalt and Ellensburg conglomerate facies immediately south of the lower fault trace, I infer the fault displacement is south side up. At Dead Cow Gulch North, the

northern range front fault system splays off into two separate fault scarps, where the younger fault strand juxtaposes Qf1 and Qf2 and the older fault strand juxtaposes Qf2 and Qf4 (Figure 7). The presence of two separate fault scarps at Dead Cow Gulch South indicates younger faulting has propagated northward as the fault splays to lower topographic levels (Figures 7 and 12).

The presence of the southern range front fault scarp is inferred from geomorphology, geologic mapping and seismic reflection data. Interpreted geometry of the southern range front fault system from seismic reflection imagery depicts a shallow ($\sim 20^\circ$) south dipping fault. The shallow dip of the fault system is corroborated by the sinuous nature of the mapped fault trace (Figure 7). Furthermore, the diffuse nature of the southern range front fault-line scarp suggests little contemporary fault activity during the late Quaternary because motion has been transferred onto the northern range front fault system. Collectively, the presence of three distinct fault lineaments documents progressive northward advancement of the range front fault system where the southern fault offsets relatively older Quaternary units, while the northernmost fault offsets the youngest alluvial unit. All three north-vergent range front faults trend across the Dead Cow Gulch South tributary (Figures 7 and 12).

No distinct fault scarp lineaments were delineated within east-of-the-canyon range front or canyon entrance through field mapping and LiDAR analysis. Based on the lack of evidence for faulting within the east-of-the-canyon range front, I infer that the north vergent range front fault system, apparent west of the canyon entrance, becomes blind (i.e., does not daylight onto the land surface) going along strike to the southeast

(Figure 6). However, a south-vergent backthrust is inferred from structural and stratigraphic observations within the canyon entrance (Figure 10). This backthrust fault trends just south of the Manastash ridgeline and is probably the same as the northeast side-up thrust fault mapped by Washington Department of Natural Resources (1992) at Vanderbilt Gap 7 km along strike to the east-southeast.

The difference in structural geometry between east-of-the-canyon range front and west-of-the-canyon range-front is exemplified by the contrasting geomorphic expression of Manastash Ridge. The Manastash Ridge east-of-the-canyon range front is a punctuated ridgeline consistent with a steeply dipping backthrusts periodically uplifting the Manastash ridgeline (Figures 6 and 10). At depth, I infer the Manastash anticline and steep forelimb (Figure 10, A-A') to be related to a ramp-flat geometry transition (Savage et al., 2003). Kinematically, the structural geometry of a north dipping backthrust truncating a syncline within the forelimb requires that slip on the backthrust would tighten the Manastash anticline and forelimb. Therefore, I suggest that uplift of the Manastash Ridge relates to fold growth of the Manastash anticline and forelimb.

In contrast, the Manastash Ridge west of the canyon entrance is a broad, flat topographic highland, which I infer reflects a gently dipping south verging ramp of the master reverse fault (Savage et al., 2003; Figure 10). Again, I suggest the Manastash anticline and forelimb to be related to a ramp flat transition at depth. While deformation is confined within the south dipping range front fault system, I assume displacement in the range front fault system to be controlled by a master fault at depth (Figure 10, B-B').

Therefore, uplift on the range front fault system would require fold growth of Manastash anticline and forelimb due to slip on the master fault.

Incision Rates of Entrenched Alluvial Deposits

Incision rates based on entrenched tributary fan deposits along the northern range front fault system ranged between 0.02 to 0.09 m/ky (Table 3). Implicit in these incision rates is the assumption that the paleo-slope of the entrenched fan deposits represents the same slope of the modern channel thalweg. However, this assumption may be invalid in at least four cases, one, if the paleo-slope steepens due to subaerial erosion following abandonment, two, if the modern slope undergoes subsequent aggradation since maximum entrenchment, three, if reverse motion on the fault system tilts the entrenched alluvial deposits, and four, if the entrenched deposits represent different fan morphology than the current thalweg morphology. Since morphologic alteration of the paleo-slope or active thalweg seems likely, another approach was used to calculate incision rates based on faults scarp height of the youngest fault scarp at Dead Cow Gulch South (Table 4). The youngest fault scarp was chosen since it documents the most recent incision. Tephrochronology analysis of Qf3 provides a minimum incision rate of 0.06 to 0.1 m/ky. Assuming the IRSL age of Ql2 (sample AM10-1 that caps Qg2) is contemporaneous with Qf2, then I calculate an incision rate of 0.07 to 0.11 m/ky. Therefore approximate incision rates along the range front are 0.06 to 0.11 m/ky over the last 100 ky (Table 4).

Comparative Incision Rates: Hanging Wall versus Footwall

Incision rates within the hanging wall of the Manastash anticline, 0.06-0.11 m/ky and 0.16-0.20 m/ky (Table 2, 3, 4) were calculated from two separate site localities where uplift of the hanging wall is a consequence of slip on the south dipping ramp master thrust (Figure 10). Hanging-wall incision rates within the core of the anticline are represented by incision of the strath terraces within the Lower Yakima River Canyon (Table 2). Incision rates from the range front fault system (Table 4) are based on the youngest fault scarp at the mouth of Dead Cow Gulch South.

The incision rate within the footwall of the Manastash range front fault is represented by lowering of the Kittitas Valley relative to the elevated remnant of the paleo valley floor at Potato Hill (Figures 3 and 16). The paleo valley floor at Potato Hill is the Ellensburg/Thorp Gravel contact, 26-40 m higher than the modern valley floor (Figure 16). Using an age for the Thorp Gravel of 3.7 My (Waitt, 1979), the lowering (incision) rate of the Kittitas Valley floor is 0.01-0.007 m/ky.

The incision rate of the hanging wall based on the strath terrace sequences (Table 2) is an order of magnitude more than the incision rate of the footwall, with the incision rate difference being about 0.15-0.19 m/ky. Assuming that the anticline incision rates are equivalent to uplift rates, I infer that the uplift rate of Manastash Ridge relative to the valley floor is on the order of 0.17 m/ky over the last 4 My (assuming that the uplift rate of the last 90 ky may be projected back in time at least until 3.7 Ma).

At the second site, which is the location of the youngest fault scarp at the mouth of Dead Cow Gulch South, the difference between incision rates (Table 4) of the hanging

wall and incision rates of the footwall are about 0.05 to 0.1 m/ky. Assuming that the incision rates are equivalent to uplift rates, I infer that the uplift rates along the range front fault system relative to the valley floor are between 0.05-0.1m/ky over the last 100 ky. Furthermore, the fault scarps ranging from 5 to 15 m high within range front fault system indicate the fault scarps must represent multiple earthquakes, and it is the resulting tectonic uplift as a consequence of such earthquakes that, over several millennia in the Quaternary, has constructed the Manastash Ridge and range front at the southern end of the Kittitas Valley.

CONCLUSIONS

In order to evaluate whether the Manastash anticline is an actively growing fold, I designed data collection and data analysis to investigate both the geomorphic evolution of the Manastash Ridge and range front and the structural growth and evolution of the Manastash anticline. Two fault scarps at the base of the Manastash range front each correlate to thrust faults evident on seismic reflection imagery across the range front west of the canyon entrance. The northernmost fault scarp cuts the youngest alluvial fan; and from the youthful appearance of the scarp, the last earthquake that freshened the scarp may be Holocene in age. Based on projection downward of the thrust faults evident on the seismic line, I infer these faults root in a south dipping master ramp thrust. Because the faults daylighting at the surface truncate Quaternary units, I infer that the Manastash anticline is an actively growing fold above a master ramp thrust. Support for the inference that the Manastash anticline is an actively growing fold is late Quaternary uplift rates within the core of the anticline, of 0.15-0.19 m/ky.

Where no faulting is observed east of the canyon entrance, successively younger fans originate at the mouth of older entrenched fan deposits and extend northward onto the valley floor. Fan growth and entrenchment is driven by episodic climatic fluctuations fostering cycles of aggradation (transport-limited conditions) and incision (supply-limited conditions).

In contrast, the range front west of the canyon entrance, contains steep and short tributaries draining off of Manastash Ridge that deposit fans at the range front junction. These fans are progressively truncated and uplifted by ongoing Quaternary faulting. Faulting isolates and uplifts fan complexes, each complex generated during climate conditions favorable to fan aggradation. Based on luminescence age determinations and tephrochronology for Manastash range front Quaternary units, I infer timing of aggradation of alluvial units (Qf3, Qf2) correlates to the late Pleistocene (Marine Isotope Stage 5) glacial-interglacial climate transition.

West of the canyon entrance, knickpoints in the short and steep tributaries are at equal elevation across several tributaries and attest that baselevel fall affects all tributaries similarly. I infer that the baselevel fall is the product of co-seismic tectonic uplift events (earthquakes) on the range front and that cumulatively over the late Quaternary these earthquakes have tightened the Manastash anticline and accommodated surface uplift of Manastash Ridge at rates of 0.15-0.19 m/ky.

REFERENCES

- Bentley, R. D., 1977, Stratigraphy of the Yakima basalts and structural evolution of the Yakima ridges in the western Columbia Plateau, in Brown, E.H. and Ellis, R.C., editors, *Geological Excursions in the Pacific Northwest: Western Washington University*, p. 339-390. Published as a geology field guide in conjunction with the 1977 annual meeting of the Geological Society of America.
- Berger, G. W. and Busacca, A. J., 1995. Thermoluminescence dating of late Pleistocene loess and tephra from eastern Washington and southern Oregon and implications for the eruptive history of Mount St. Helens: *Journal of Geophysical Research*, v. 100, p. 22361–22374.
- Blakely, R. J., Sherrod, B. L., Weaver, C. S., Wells, R. E., Rohay, A. C., Barnett, E. A. and Knepprath, N. E., 2011, Connecting the Yakima fold and thrust belt to active faults in the Puget Lowland, Washington: *Journal of Geophysical Research*, v. 116, B07105, 33 p.
- Bull, W. B., 1991, *Geomorphic responses to climatic change*: Oxford University Press, 326 p., ISBN 0-19-505570-5.
- Campbell, P.C. and Bentley, R.D., 1981, Late Quaternary Deformation of the Toppenish Ridge Uplift in south-central Washington; *Geology*, v. 9, p. 519-524.
- Harvey, A. M., Wigand, P. E. and Wells, S. G., 1999, Response of alluvial fan systems to the late Pleistocene to Holocene transition: Contrasts between the margins of pluvial lakes Lahontan and Mojave, Nevada and California, USA: *Catena*, v. 36, p. 255-281.
- Kirby, E. and Whipple, K., 2001, Quantifying differential rock-uplift rates via stream profile analysis; *Geology*, v. 29, p. 415-418.
- Morthekai, P., Jain, M., Cunha, P. P., Azevedo, J. M. and Singhvi, A. S., 2011, An attempt to correct for fading in million year old basaltic rocks: *Geochronometrika*, v. 38(3), p. 223-230.
- Porter, S. C., 1976, Pleistocene glaciation in the southern part of the North Cascade Range: Washington, *Geological Society of America Bulletin*, v. 87, p. 61-75.
- Price, E. H. and Watkinson, A J., 1989, Structural geometry and strain distribution within eastern Umtanum fold ridge, south-central Washington, in Reidel, S. P., and

- Hooper P.R., editors, Volcanism and Tectonism in the Columbia River flood-basalt province: Geological Society of America Special Paper 239, p. 265-281.
- Reidel, S.P., 1984, The Saddle Mountains: The Evolution of an Anticline in the Yakima Fold Belt; *American Journal of Science*, v. 284, p. 942-978.
- Reidel, S. P., Campbell, N. P., Fecht, K. R. and Lindsey, K. A., 1994, Late Cenozoic structure and stratigraphy of south-central Washington, in Lasmanis, R. and Cheney, E.S., conveners, *Regional Geology of Washington State: Washington Division of Geology and Earth Resources Bulletin 80*, 159-180.
- Ritter, J. B., Miller, J. R., Enzel, Y. and Wells, S. G., 1995, Reconciling the roles of tectonism and climate in Quaternary fan evolution: *Geology*, March v. 23; p. 245-248.
- Savage, H. M., and Cooke, M. L., 2003, Can flat-ramp-flat geometry be inferred from fold shape?: A comparison of kinematic and mechanical folds: *Journal of Structural Geology*, v. 25, p. 2023-2034.
- Schumm, S. A., 1993, River response to baselevel change: implications for sequence stratigraphy: *Journal of Geology*, v. 101, p. 279-294.
- Smith, G. A., 1998, Neogene synvolcanic and syntectonic sedimentation in central Washington; *Geological Society of America Bulletin*, v. 100, p. 1479-1492.
- Snyder, N. P., Whipple, K. X., Tucker, G. E. and Merritts, D. J., 2000, Landscape response to tectonic forcing: Digital elevation model analysis of stream profiles in the mendocino triple junction region, northern California, *Geological Society of America Bulletin*, v. 112, p. 1250-1263.
- Spelz, R. M., Fletcher, J. M., Owen, L. A. and Caffee, M. W., 2008, Quaternary alluvial-fan development, climate and morphologic dating of fault scarps in Laguna Salada, Baja California, Mexico: *Geomorphology*, vol. 102, 578-594.
- Sweeney, M.R., Busacca, A.J., Gaylord, D.R., 2005, Topographic and climate influences on accelerated loess accumulation since the last glacial maximum in the Palouse, Pacific Northwest, USA; *Quaternary Research* 63 (2005) 261-273.
- Tolan, T. L., Martin, B. S., Reidel, S. P., Anderson, J. L., Lindsey, K. A. and Burt, W., 2009, An introduction to the stratigraphy, structural geology, and hydrology of the Columbia River Flood-Basalt Province: a primer for the GSA Columbia River Basalt Group field trips; *Volcanoes to Vineyards, Geologic Field Trips through*

the Dynamic Landscape of the Pacific Northwest; Geological Society of America Field Guide 15, p. 599-643.

Waitt, R. B., 1979, Late Cenozoic deposits, landforms, stratigraphy and tectonism in Kittitas Valley, Washington, U. S. Geological Survey Professional Paper 1127, 18 p.

Washington Department of Natural Resources (1994), Washington geologic maps, 1:100,000 scale, Yakima sheet:
http://www.dnr.wa.gov/Publications/ger_geologic_maps_wa.pdf

Wells, R. E., C. S. Weaver, R. J. Blakely, 1998. Forearc migration in Cascadia and its neotectonic significance: *Geology*, v. 26, p. 759-762.

West, M. W., Ashland, F. X., Busacca, A. J., Berger, G. W. and Shaffer, M. E., 1996, Late Quaternary Deformation, Saddle Mountain Anticline, south-central Washington: *Geology*, v. 24, p.1123-1126.

Whipple, K. X, Wobus, C., Crosby, B., Kirby, E., Sheelan, D., 2007, New Tools for Quantitative Geomorphology: Extraction and Interpretation of Stream Profiles from Digital Topographic Data; GSA Annual Meeting 2007.

Whitlock, C., Sarna-Wojcicki, A. M., Bartlein, P. and Nickmann. R. J., 2000, Environmental history and tephrostratigraphy at Carp Lake, southwestern Columbia Basin, Washington, USA, *Palaeogeography, Palaeoclimatology, Palaeoecology* v. 155, p. 7-29.

Wobus, C., Whipple, K. X., Kirby, E., Snyder, N., Johnson, J., Crosby B., Sheehan, D., 2006, Tectonics from topography: Procedures, promise, and pitfalls; *Geological Society of America Special Paper* 398, p 55-74.

Wobus, C., Crosby, B., Kirby, E., Sheehan, D., Whipple, K., Snyder, N., Ouimet, W., Gasparini, N., Dibase, R., 2008, *GSA Short Course: Tectonic Geomorphology*

Zaprowski, B. J., Pazzaglia, F.J. and Evenson, E.B., 2005, Climatic influences on profile concavity and river incision: *Journal of Geophysical Research*, v. 110, F03004, doi:10.1029/2004JF000138.

Tables

Table 1. Infrared stimulated luminescence (IRSL) K-feldspar ages, Manastash anticline, Washington (analyses by Shannon Mahan, USGS, Denver, CO)

Location	Elevation (m)	Geologic unit	Sample identification number	Equivalent dose (Gy)	IRSL age (yrs) Fade corrected*
Yakima Canyon	450	Q12 loess**	AM10-1	235 ± 10.6	$88,750 \pm 4,520$
Yakima Canyon	484	Qg4 fluvial gravel	AM 10-2	102 ± 5.54	$45,000 \pm 2,900$ $254,250 \pm 17080^*$
Shushuskin fan	495	Qf4 fan gravel	MN10-1	108 ± 11.3	$47,890 \pm 5,340$ $279,020 \pm 31,240^*$
Dead Cow Gulch	494	Qf4 fan gravel	MN10-3	93.7 ± 3.94	$41,810 \pm 2,140$ $228,220 \pm 11,900^*$
Dead Cow Gulch	494	Qf4 fan gravel	MN10-4	94.3 ± 3.03	$40,240 \pm 1880$ $215,880 \pm 10,310^*$
Spring Canyon	514	Qf3 loess	MN10-5	60.7 ± 3.96	$20,860 \pm 1520$

*Assumes an anomalous fade rate of 13% (13% fade rate after Morthekai et al., 2011).
Anomalous fading of K-feldspars: an observation that the field saturation luminescence intensity is less than the laboratory saturation intensity because of electron “tunneling” from principal luminescence traps to nearby structural defects in sediment in field situations.

** Q12 loess overlies Qg2 alluvium - see Figure 8.

Table 2. Incision rates using uplifted strath terraces, Lower Yakima River Canyon entrance, Manastash anticline

Geologic unit	Site number*	Surface elevation (m)	Elevation of strath (m)	Elevation, modern thalweg (m)	Amount of incision (m)	Sample age, IRSL** (ky)	Incision rate (m/ky)
Q12	AM10-1	448	442	427	15	84.2-93.3	0.16-0.18***
Qg4	AM10-2	478	476	428	48	237-271	0.18-0.20****

* See Table 1.

** Fade corrected, see Table 1.

*** Because the IRSL age constrains the age of the capping loess (Q12) and the underlying alluvial gravel (Qg2) is 2 m deeper, these incision rates are maximum limiting and the actual incision rate may be less.

**** Maximum incision rate - the actual incision rate is probably lower because luminescence age provides only a lower bound to age of Qg4.

Table 3. Incision rates using entrenched tributary alluvial fans, west-of-the-canyon range front, Manastash Ridge

Tributary Name	Geologic unit	Fan surface elevation (m)	Elevation of thalweg (m)	Amount of incision (m)	Sample age* (ky)	Incision rate (m/ky)
Spring Cyn	Qf4	487	468	20	206-310**	0.06-0.09***
Dead Cow Gulch South	Qf2	460	452	8	100	0.08
Long Tom Canyon	Qf4	492	486	6	206-310**	0.02-0.03***

* See Table 1.

** Maximum and minimum ages were calculated based fade corrected IRSL analyses of samples MN10-1, MN10-3, MN10-4.

**** Amount of vertical incision divided by maximum age. Due to the IRSL fade correction, the minimum incision rate yields the lower bounds of the maximum incision rate.

Table 4. Incision rate calculations using fault scarp height within the range front fault system, Dead Cow Gulch South, Manastash Ridge

Fault Trace	Constraining Geologic Unit	Fault Scarp Height (m)***	Sample age (ky)	Incision rate (m/ky)****
Lower northern fault scarp	Qf2	6-10	100*	0.06-0.1
			90**	0.07-0.11

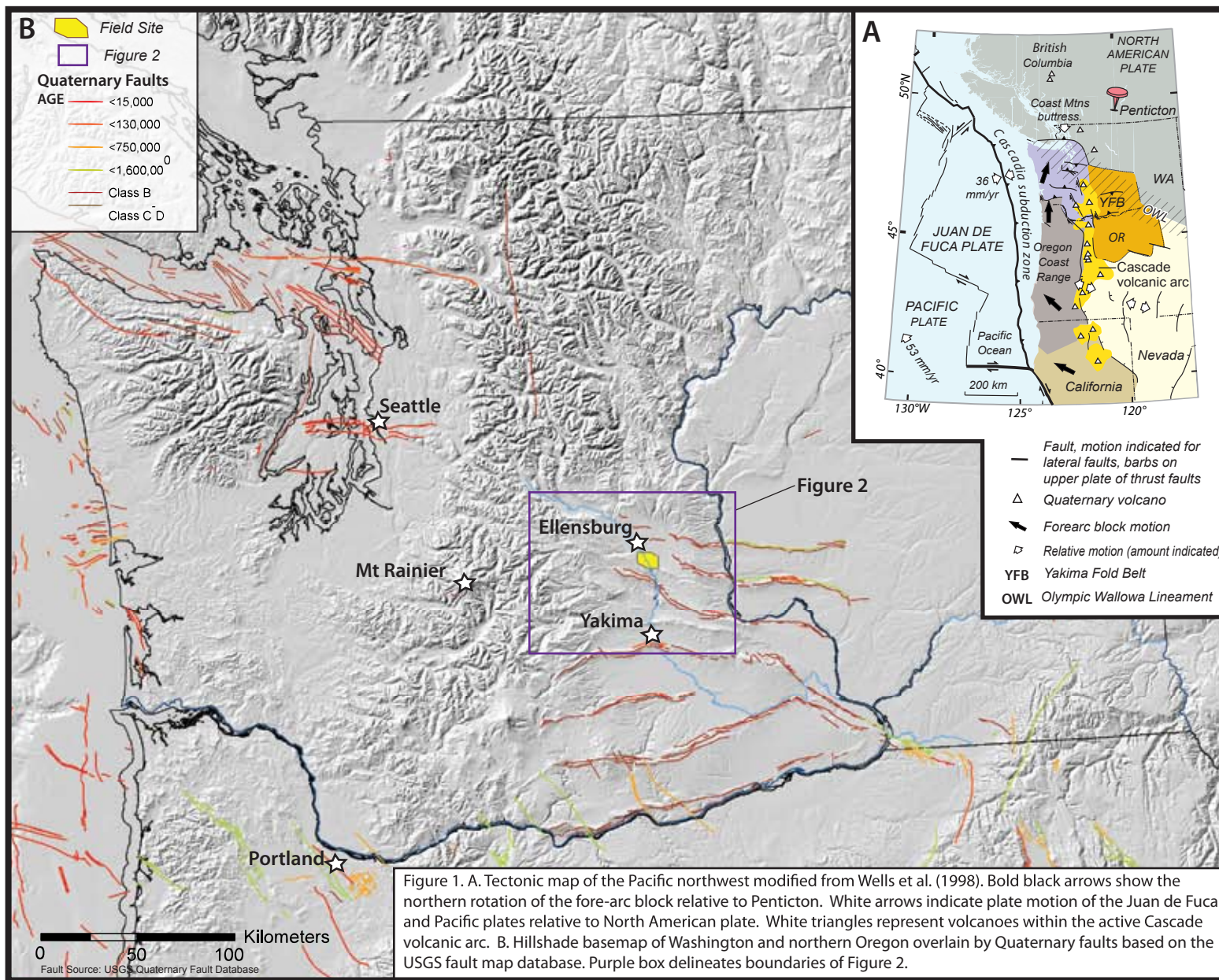
*Based on tephrochronology

**Based IRSL sample AM10-1, Table 1

*** Height of fault scarp determined from LiDAR analysis and MATLAB.

**** Amount of vertical incision divided by maximum age.

FIGURES



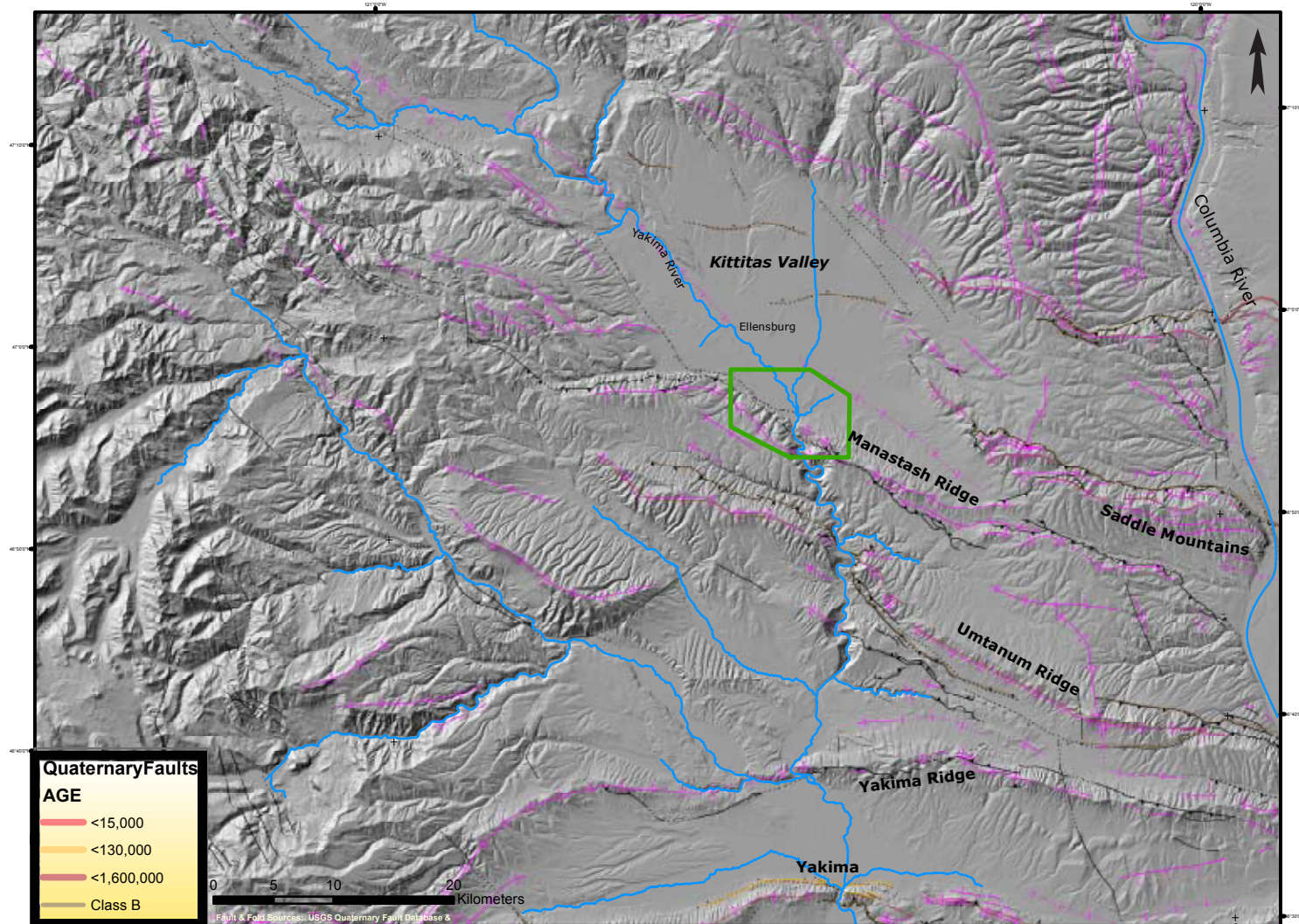


Figure 2. A 10-meter digital elevation model (DEM) of the northwestern sub-province of the Yakima Fold Belt, illustrating the Kittitas Valley, Manastash, Umtanum and Yakima ridges and lower Yakima River Canyon. Green polygon delineates study area. Purple and black lines indicate fold axes and faults mapped by Washington State Department of Natural Resources (1992). Red, yellow, maroon, and brown lines represent approximate ages of Quaternary faults within the field area and surrounding region (USGS Quaternary Fault Database). Blue lines represent the major drainage network. The ridgelines approximately define strike of anticline axes within the Yakima Fold Belt. The broadly defined western boundary of the Yakima Fold Belt is identified by the gradual transition from east-west or northwest-southeast ridges trends of the fold belt westward to the mountainous topography of the Cascade Range.

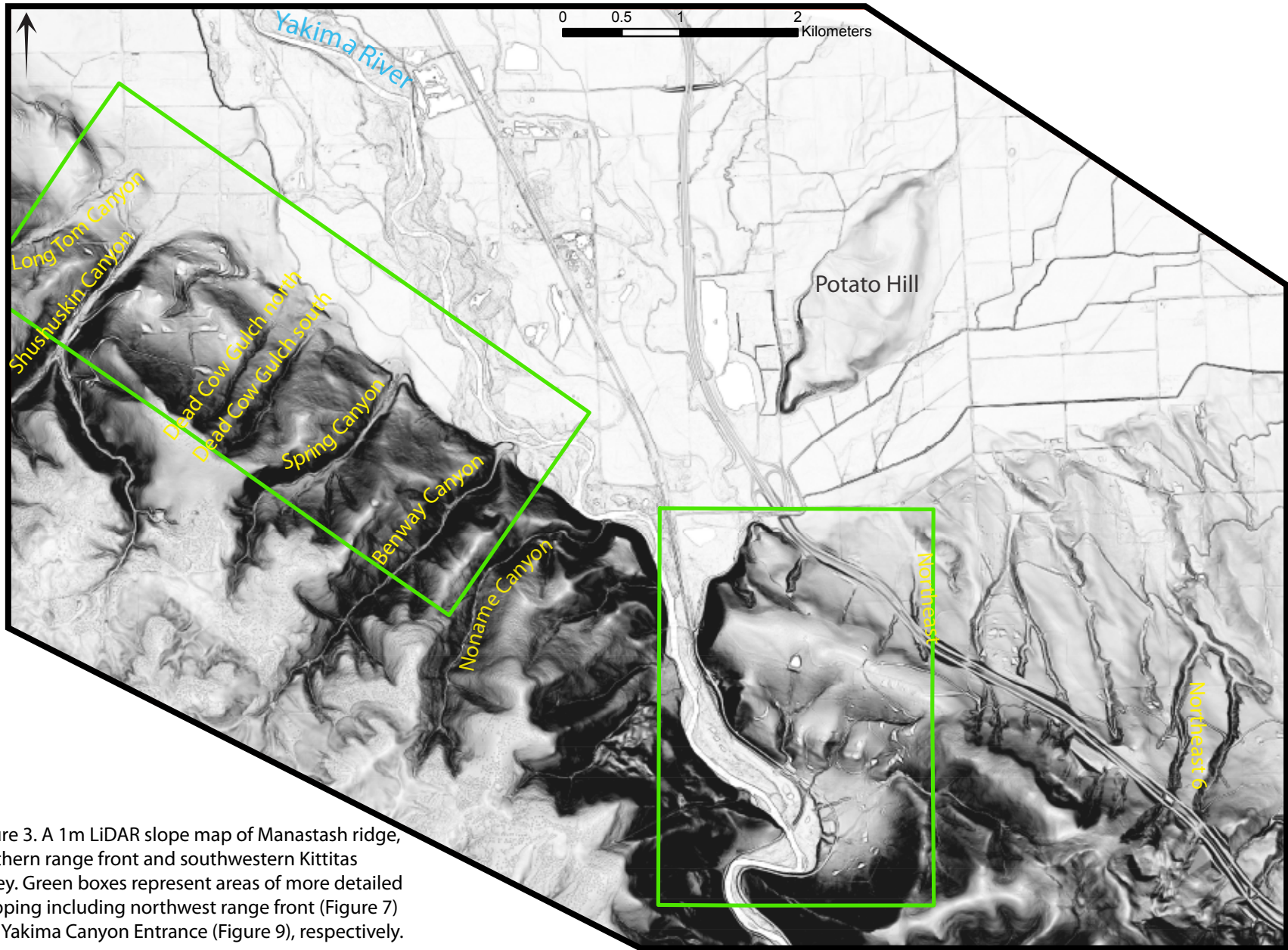


Figure 3. A 1m LiDAR slope map of Manastash ridge, northern range front and southwestern Kittitas Valley. Green boxes represent areas of more detailed mapping including northwest range front (Figure 7) and Yakima Canyon Entrance (Figure 9), respectively.

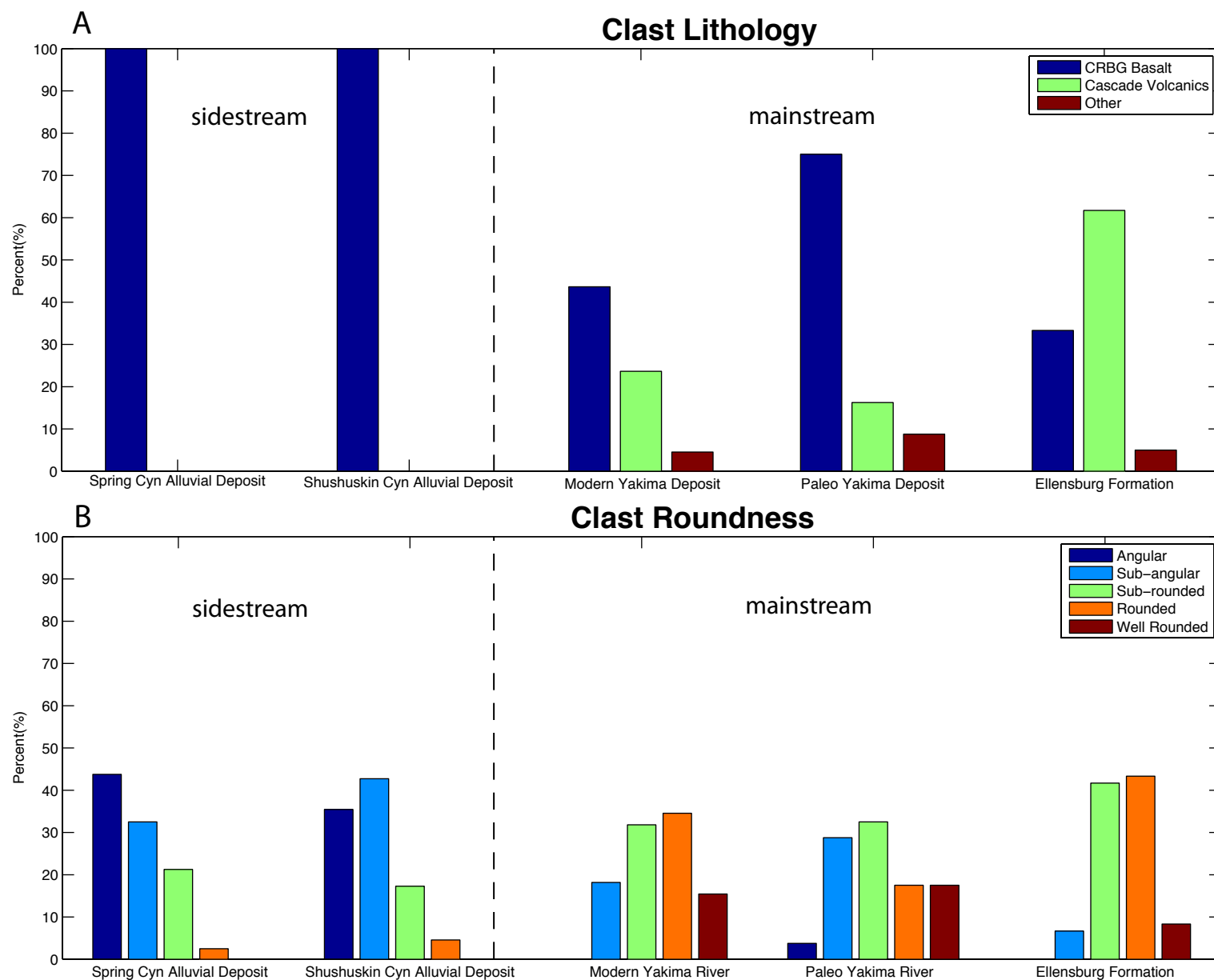
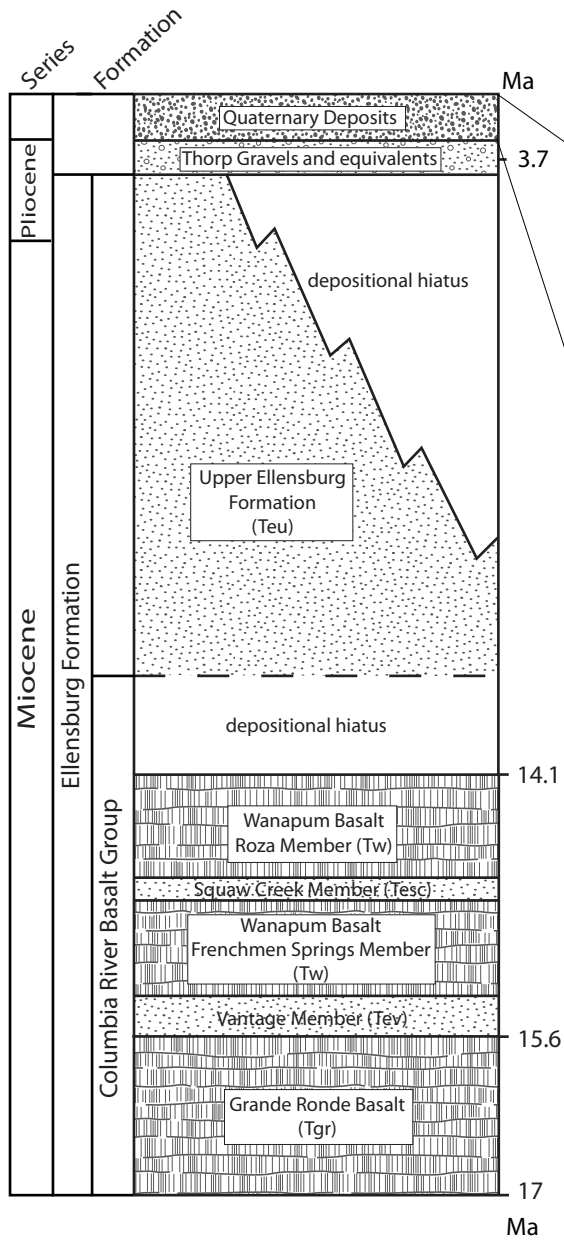


Figure 4. A. Histograms of clast lithology from five different alluvial units. B. Histograms of degree of clast roundness from five different alluvial units



Quaternary deposits in the vicinity of Manastash Ridge range-front and Entrance to lower Yakima River Canyon

Increasing Relative Age ↓	Yakima River alluvium “Mainstream” facies of Waitt (1979)		Tributary fan alluvium “Sidestream” facies of Waitt (1979)		Undifferentiated alluvial deposits	Loess		Landslide deposits
	Modern alluvium	Qal	Modern alluvium	Qal				
	Holocene alluvium	Qoal	Modern fan deposits	Qf1				
	Alluvial terrace gravel (Pleistocene)	Qg2	Older fan deposits (Late Pleistocene)	Qf2	Qfu	Ql2	Qlu	Qls
				Qf3				
		Qg4		Qf4				
		Qg5		Qf5				
		Qg6		Qf6				
			Qf7					

Figure 5. Regional stratigraphic column of the southwest Kittitas Valley modified from Smith (1988) delineating the relationship between the Columbia River Basalt Group and the Ellensburg Formation. Expanded table illustrates the Quaternary lithofacies employed within this study for the Manastash range front and lower Yakima River Canyon.

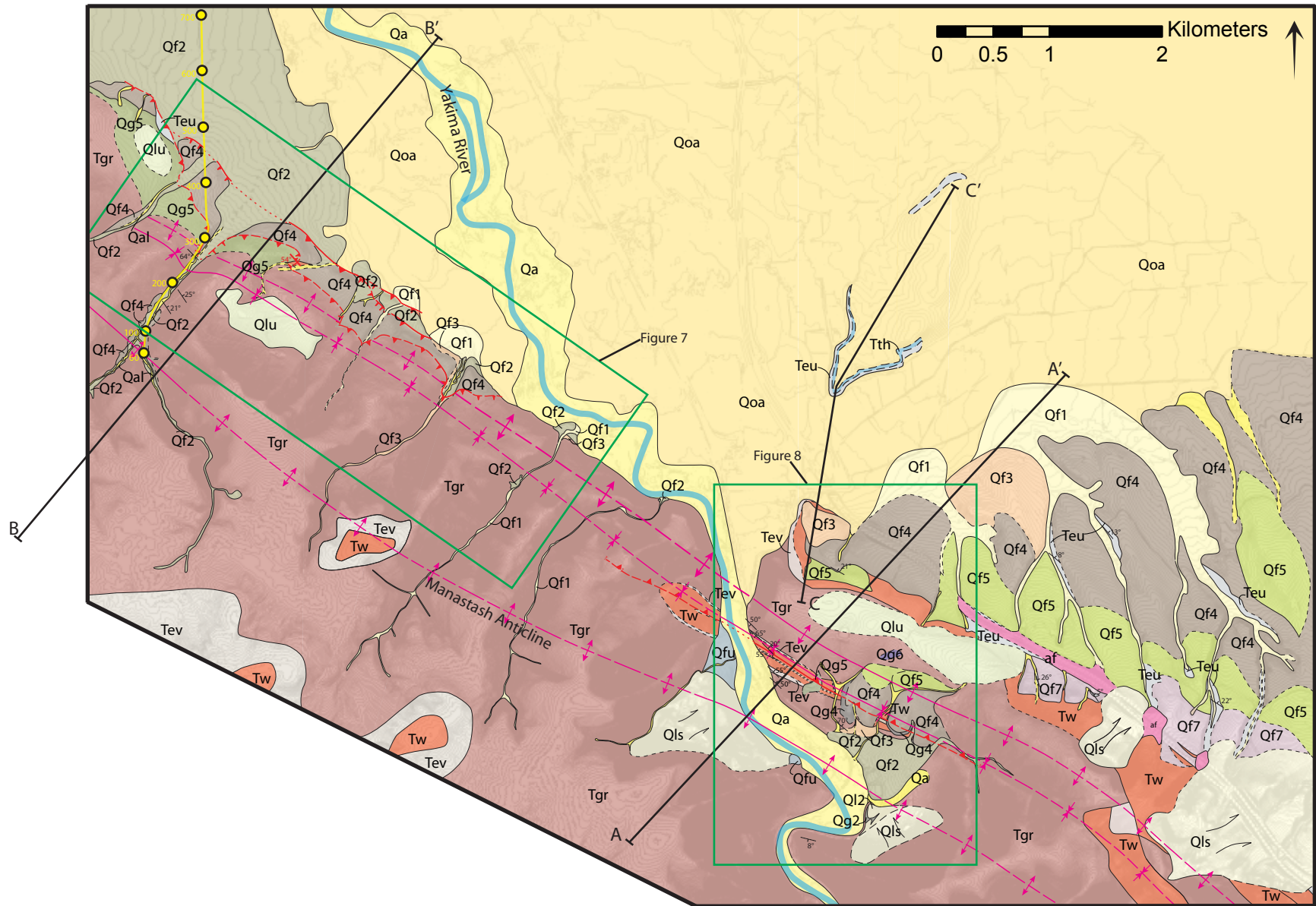
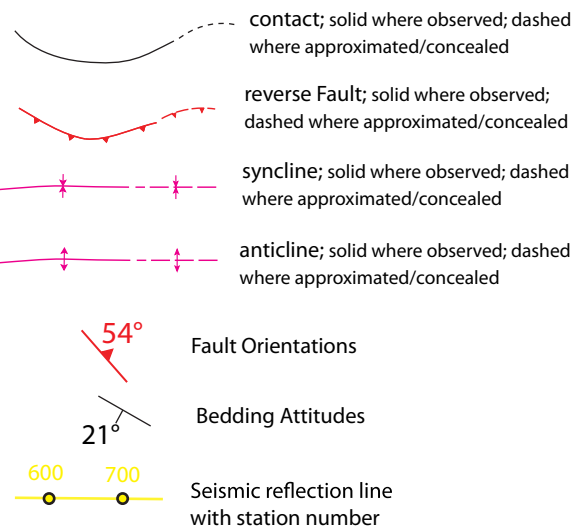


Figure 6. A. Geologic map of the northern range front of Manastash Ridge and the southern Kittitas Valley, central Washington. Contour interval 2 m. Yellow line represents the location of the seismic reflection imagery; yellow dots are the seismic station numbers. Bedrock mapping beyond the green and blue boxes, including the southwestern edge of cross section B-B', was adapted from the Yakima Quadrangle 1:100,000 scale geologic map (Washington Department of Natural Resources, 1978). B. Legend for the geologic map depicted in Figure 6A.

Geologic Symbols



Geologic Units

af artificial fill	Qf5 Quaternary fan deposit 5
Qa Modern Yakima River alluvium	Qg5 Quaternary paleo-Yakima River gravel 5
Qal Modern alluvium	Qg6 Quaternary paleo-Yakima River gravel 6
Qoa Older Yakima River alluvium	Qf7 Quaternary fan deposit 7
Qls Quaternary landslide deposit	Qlu Quaternary loess undifferentiated
Qf1 Quaternary fan deposit 1	Qfu Quaternary fan deposits undifferentiated
Ql2 Quaternary loess deposit 2	Tth Thorp Gravel
Qf2 Quaternary fan deposit 2	Teu Upper Ellensburg Formation
Qg2 Quaternary paleo-Yakima River gravel 2	Tw Columbia River Basalt Group, Wanapum
Qf3 Quaternary fan deposit 3	Tesc Ellensburg Formation, Squaw Creek Member
Qf4 Quaternary fan deposit 4	Tev Ellensburg Formation, Vantage Member
Qg4 Quaternary paleo-Yakima River gravel 4	Tgr Columbia River Basalt Group, Grand Ronde

Figure 6B

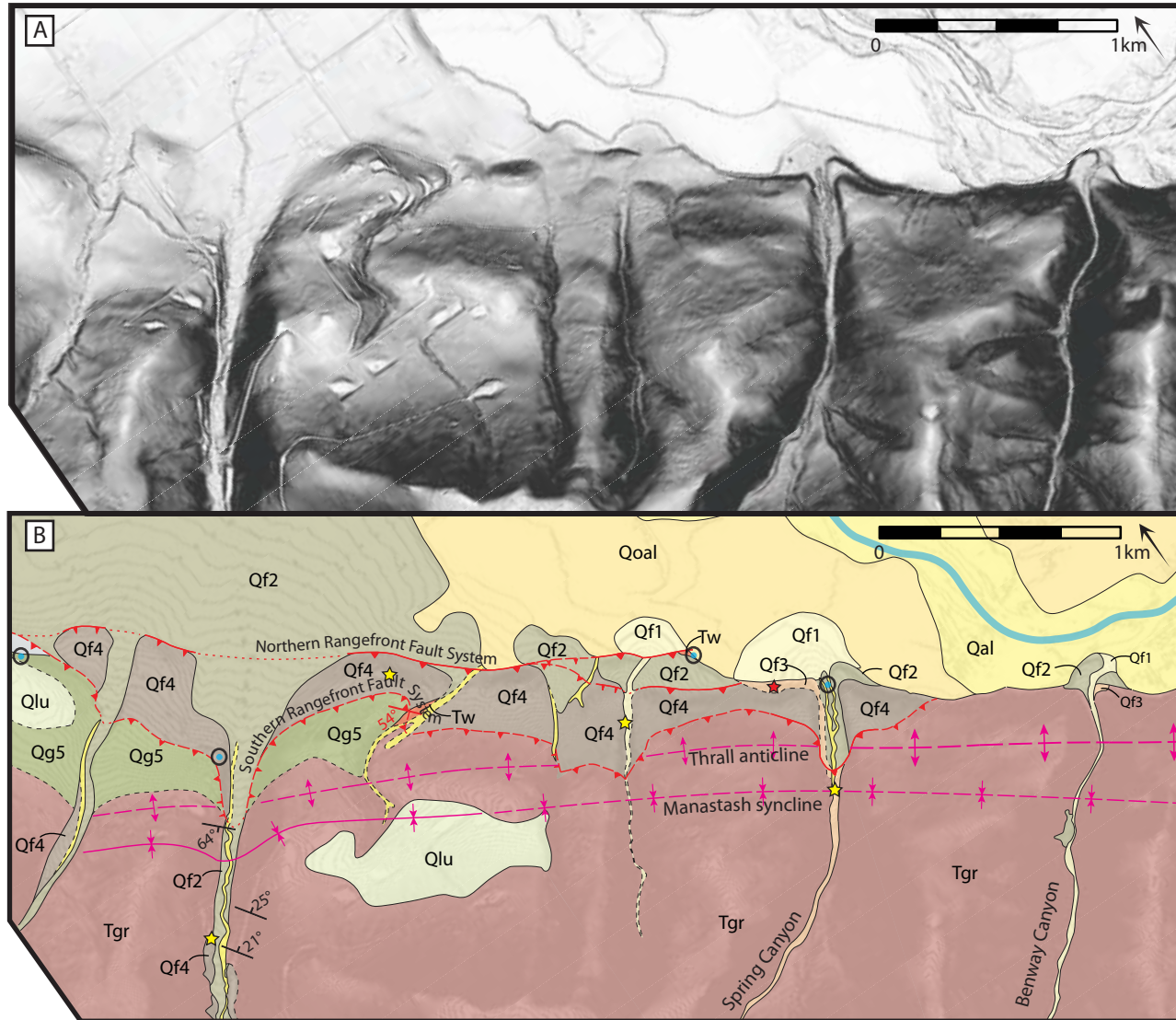


Figure 7. A. Oblique LiDAR (1m) slope map of the western range front of Manastash Ridge extending from Long Tom Canyon in the northwest to Benwy Canyon in the southeast. B. Companion geologic map of the western Manastash range front. See Figures 4 and 6 for unit and geologic symbol descriptions. Pebble and cobble count sample locations are noted by black circles with blue centers. Location of the modern Yakima River cobble count sample location is beyond the limits of the map. Red and yellow stars depict sample locations for Tephra and IRSL analyses, respectively. Contour interval 2m.

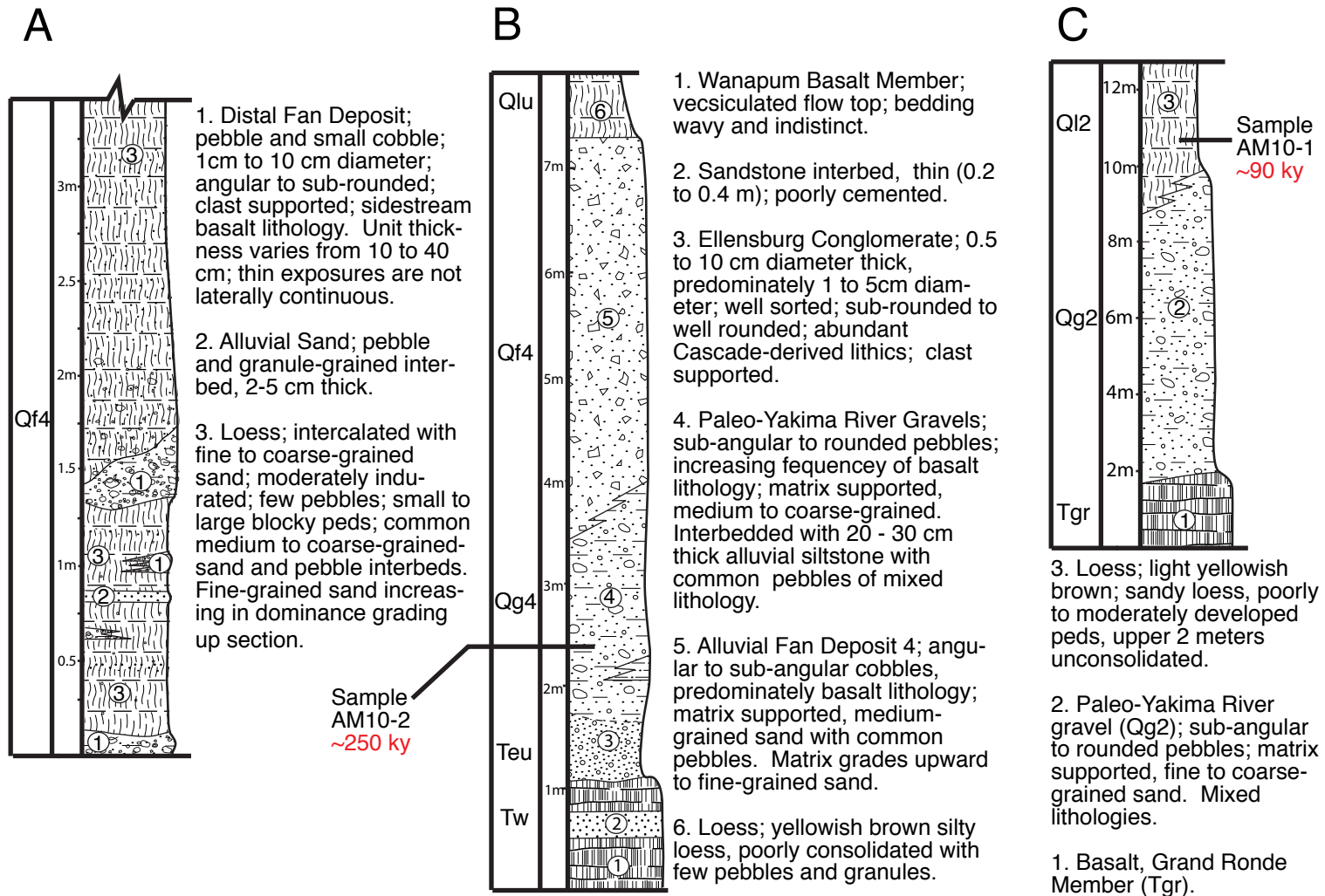


Figure 8. Stratigraphic columns of Quaternary units within the west-of-the-canyon range front and Yakima River Canyon. A. Composite stratigraphic section near mouth of Spring Canyon, B. Composite stratigraphic section of strath terrace sequence Qg4/Qf4/Qu in northern portion of abandoned meander, C. Composite stratigraphic section of strath terrace sequence Qg2 overlain by Ql2 in southern portion of abandoned meander.

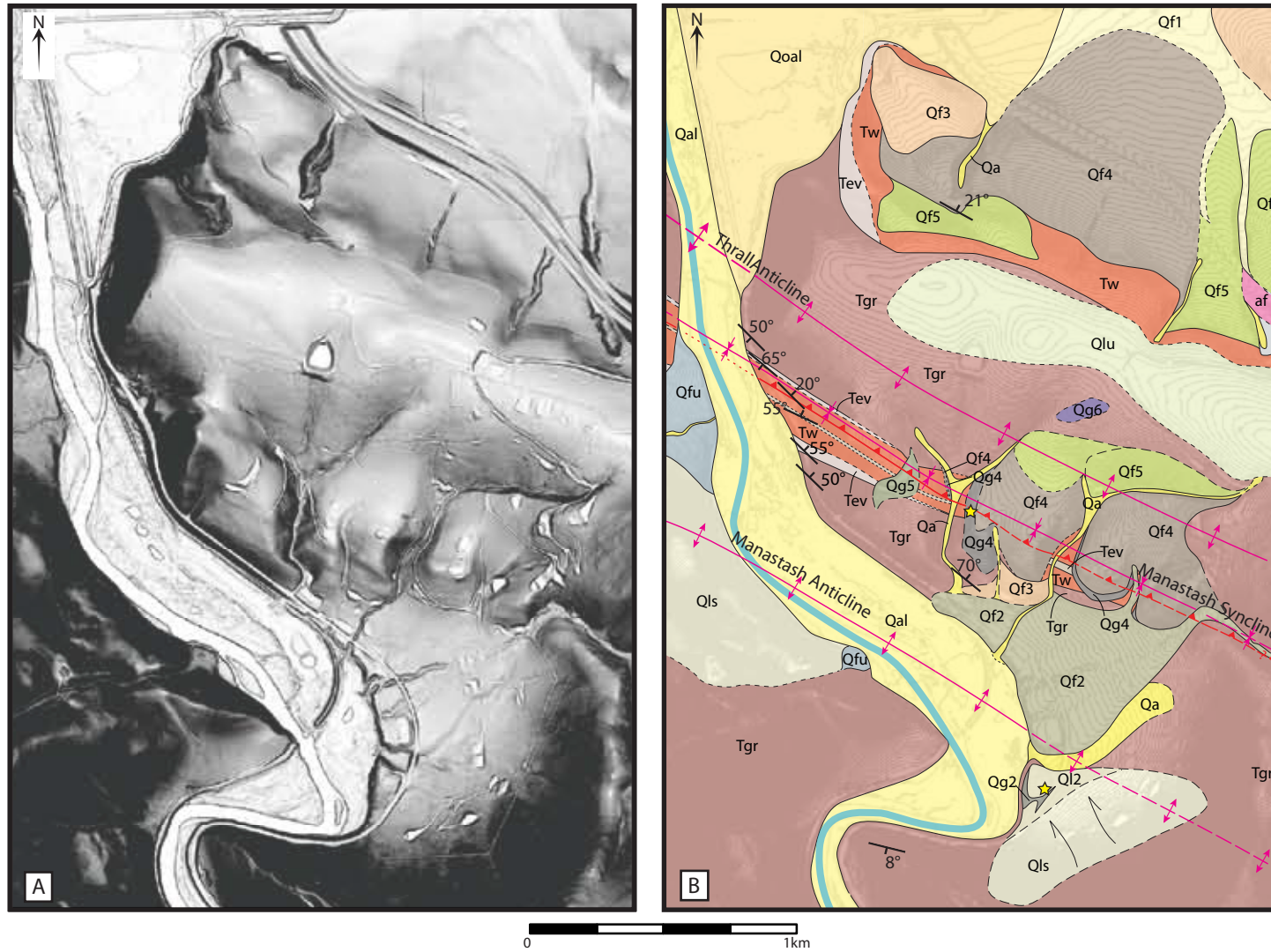


Figure 9. A. LiDAR (1 m resolution) slope map of the Yakima Canyon entrance extending southward across Manastash ridge into the lower Yakima River Canyon. B. Companion geologic map of the canyon entrance and adjacent areas. Blue line represents the south flowing Yakima River. See Figures 4 and 6 for unit and geologic symbol descriptions. Yellow stars depict sample locations for IRSL analyses. Contour interval 2 m.

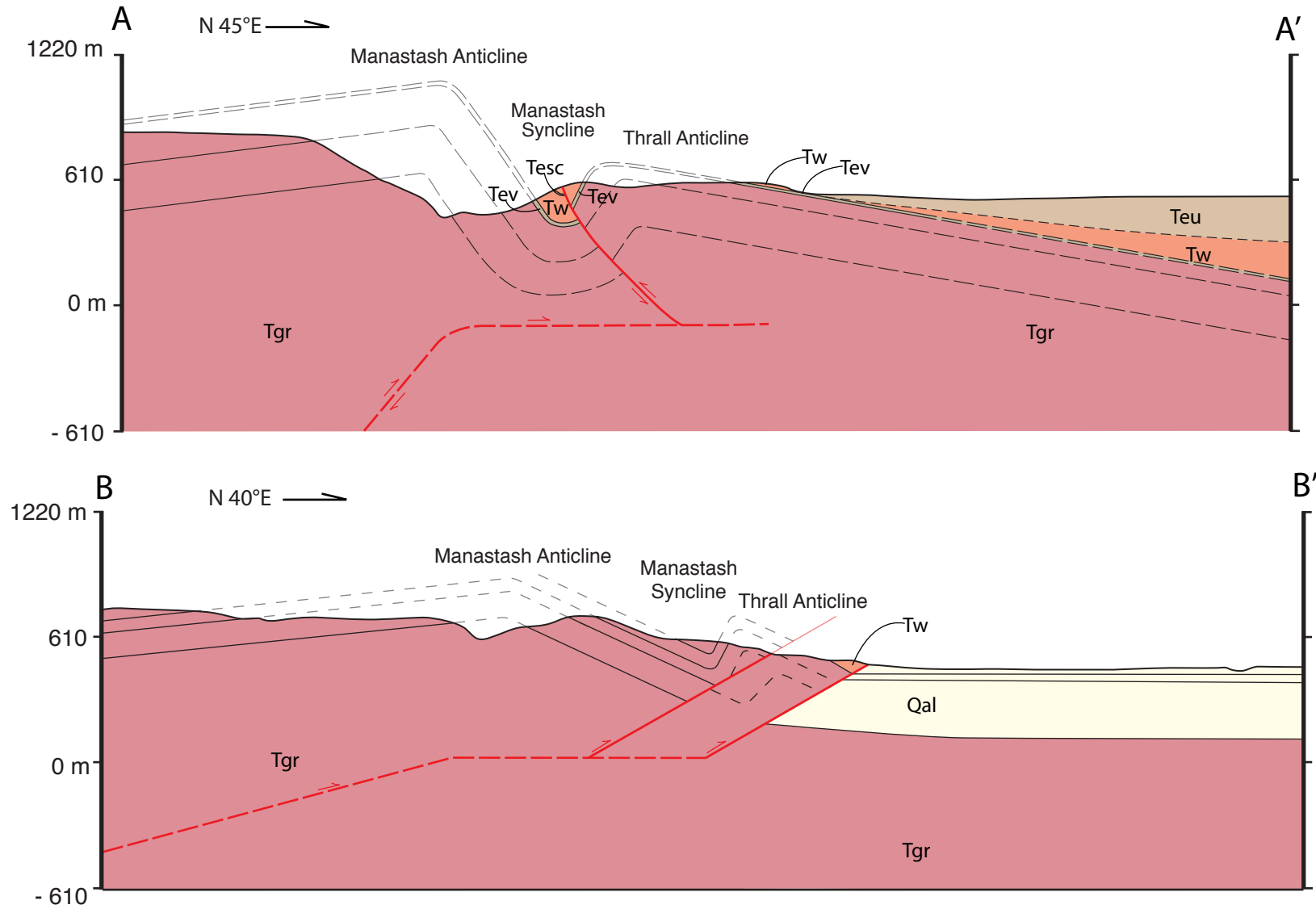


Figure 10. Geologic cross sections, no vertical exaggeration. Cross section A-A' extends northwest from Manastash Ridge to Kittitas Valley within the vicinity of the Lower Yakima River Canyon entrance. Cross section B-B', which is adjacent to Shushuskin Canyon, extends northwest from Manastash Ridge to Kittitas Valley. Geologic units within the Ellensburg Formation (Figure 5): Tgr, Grand Ronde basalt member; Tev, Vantage clastic member; Tw, Wanapum basalt member; Tesc, Squaw Creek clastic member; Teu, Upper Ellensburg Formation.

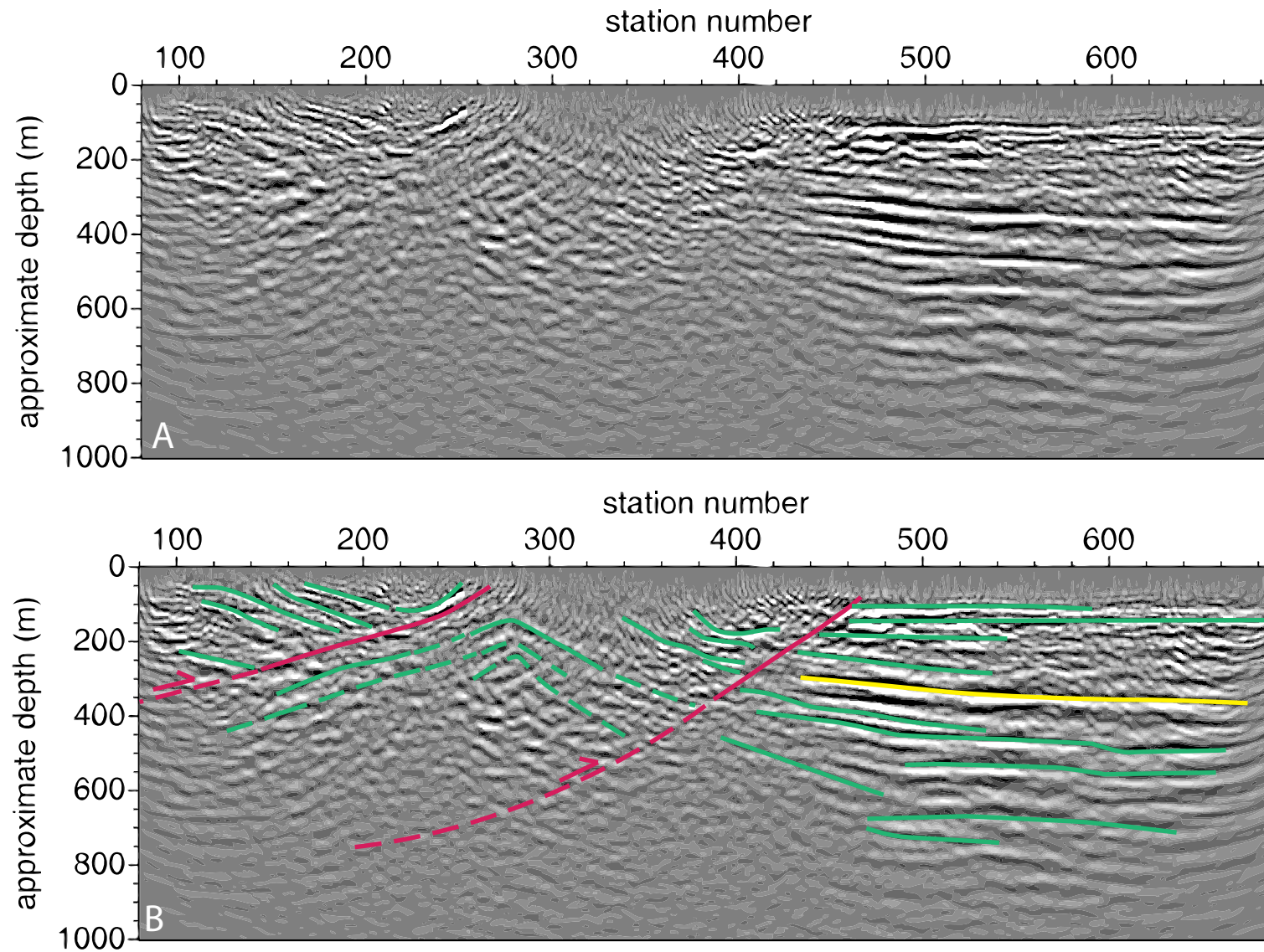


Figure 11. A. Migrated seismic reflection imagery along Umtanum road. Seismic reflection line trends northwest within Shushuskin Canyon from stations 0 to 300 and then extends northwest onto the alluvial sediments between stations 300 to 700. B. Interpreted migrated seismic reflection imagery. Green lines represent bedding, red lines represent faults and yellow line delineates the transition between Quaternary alluvial sediment and Grand Ronde Basalt of the Columbia River Basalt Group.

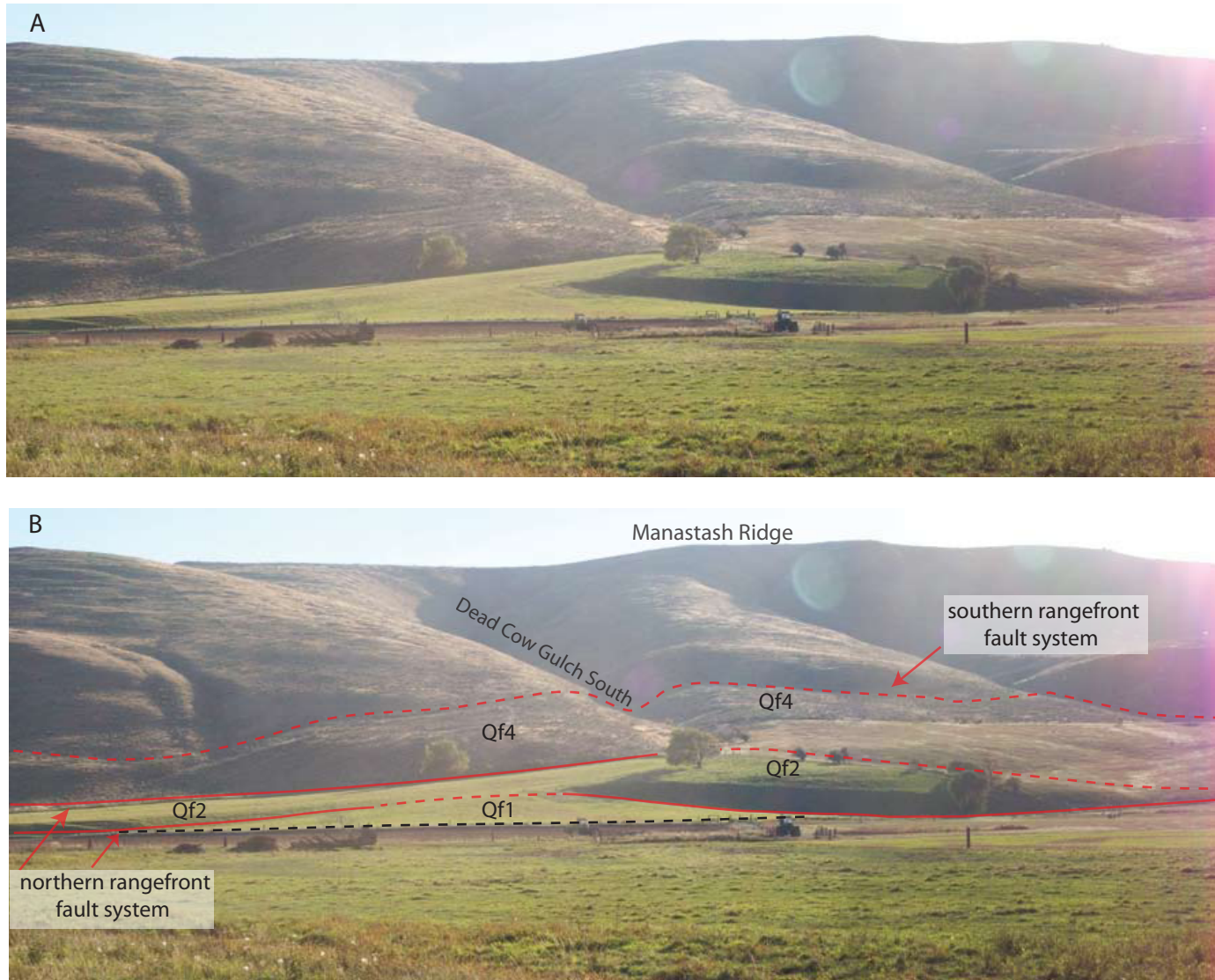


Figure 12. A. Southerly oriented photograph of Manastash range front west of the canyon entrance at tributary Dead Cow Gulch South. B. Annotated photograph of the Manastash range front with fault scarps delineated by a red line, contact dashed where approximated or indistinct. Alluvial contact noted by black line, contact dashed where approximated or indistinct. Note tractor in foreground for approximate scale.

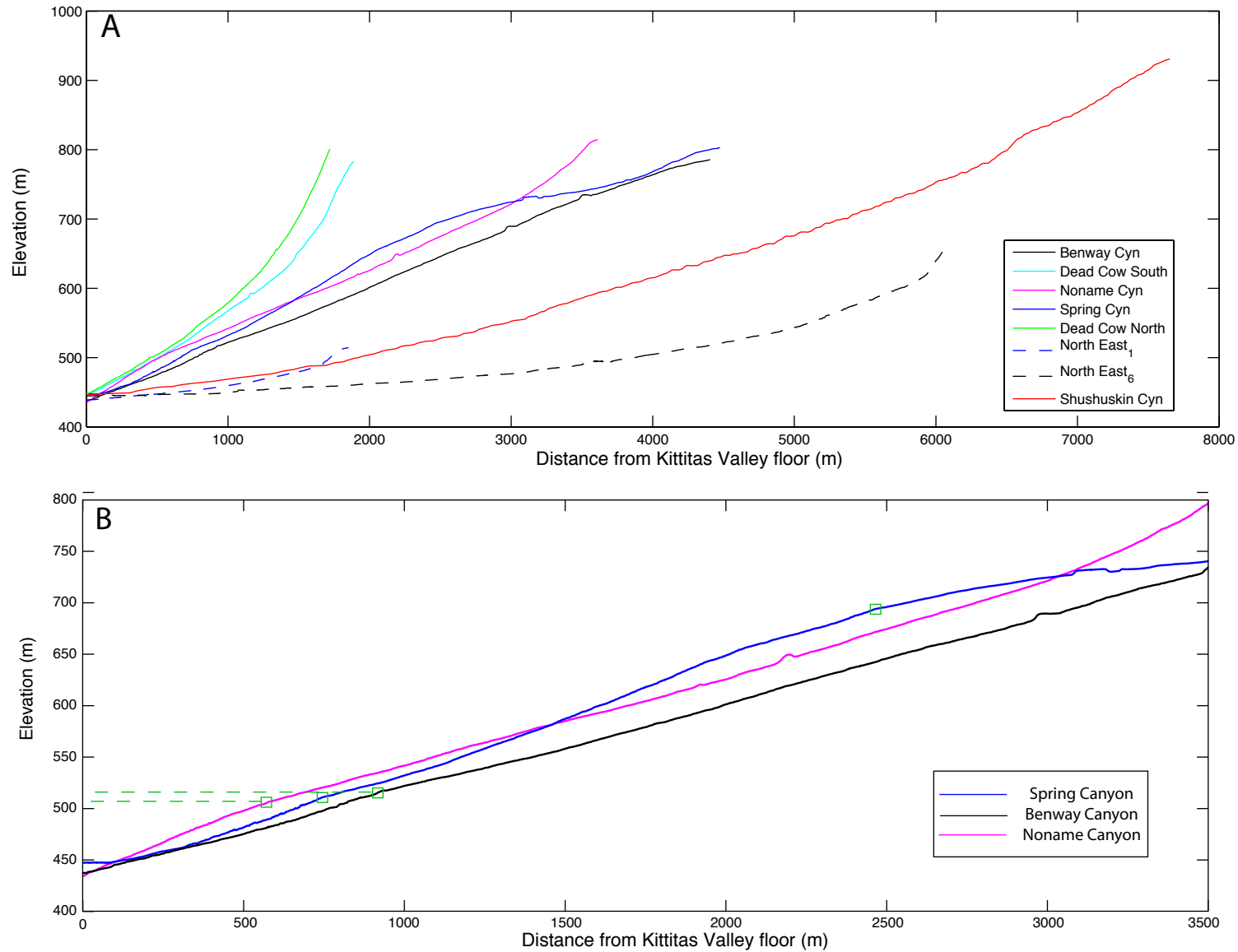


Figure 13. A. Longitudinal profiles of the Manastash range front tributaries. Dashed lines represent tributaries situated in the eastern range front. B. Longitudinal profiles of Spring, Benwy and Noname canyons. Green boxes indicate corresponding knickpoints. Note coincident knickpoint elevations range approximately at 510 m.

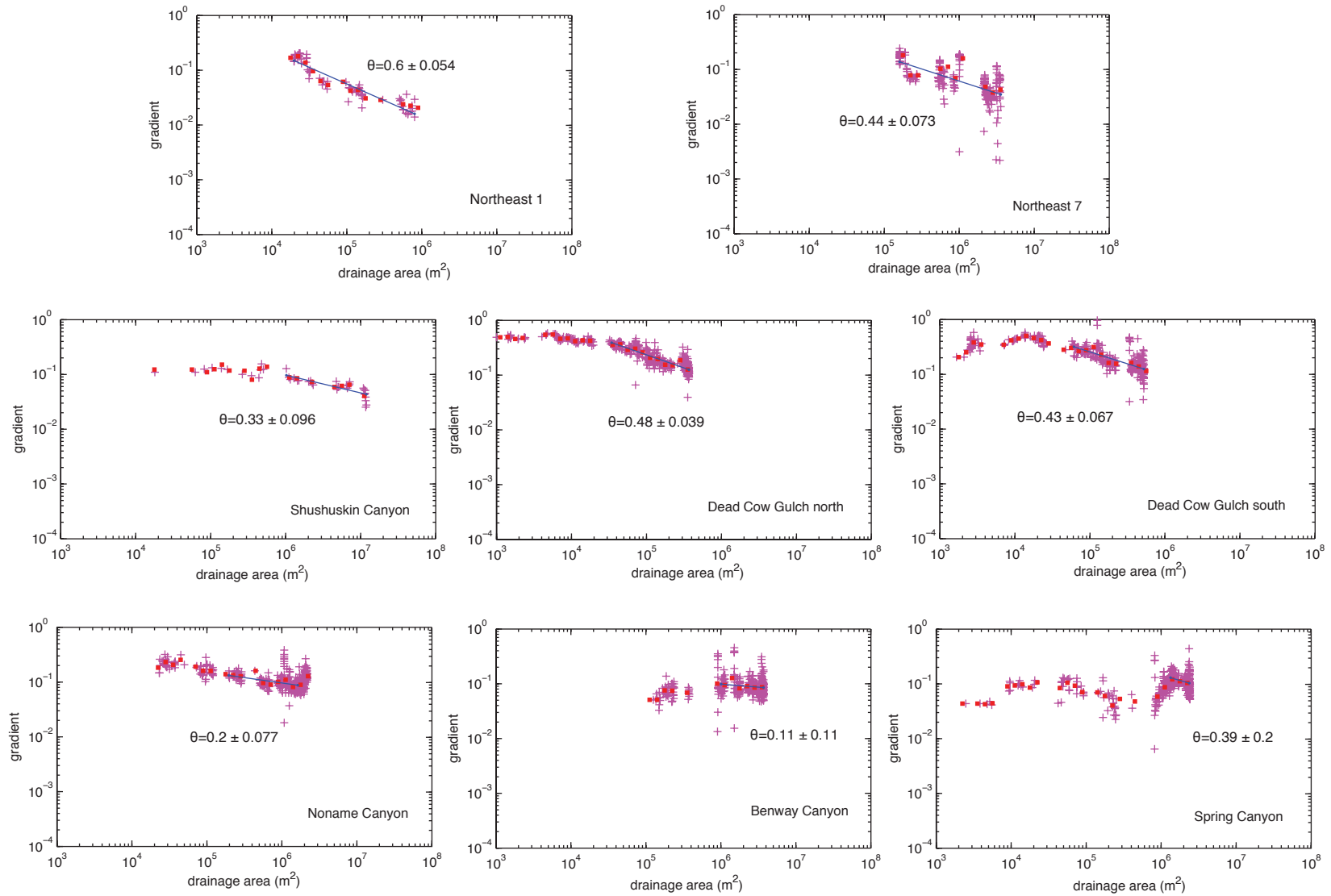


Figure 14. Slope-drainage area plots for the range front tributaries. All plots use raw slope and area data. For LiDAR-based DEMs, data extraction interval was 1 m. The one exception was the 10-m-DEM basis for the Shushuskin Canyon data, where the extraction interval was 12.41 m and the plots used a smoothing window of 250 m.

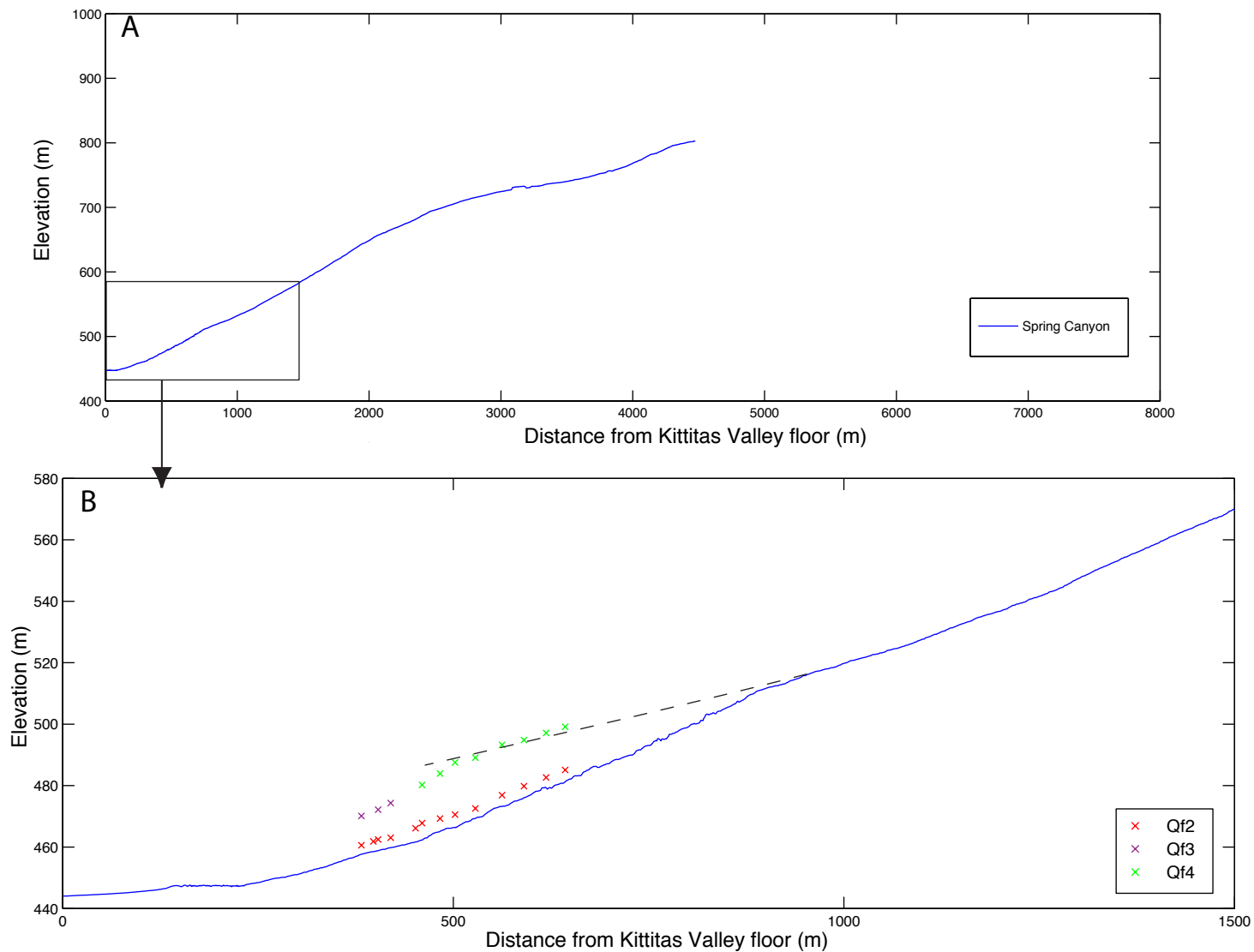


Figure 15. A. Longitudinal profile of Spring Canyon. B. Longitudinal profile of just the lower reach of Spring Canyon. Point elevations from each alluvial unit (Qf2, Qf3, Qf4) were projected horizontally onto the vertical plane containing the channel thalweg thereby defining fan surface elevations above the tributary thalweg. Relict profile (dashed line) projected downstream from knickpoint to alluvial fan surface Qf4.

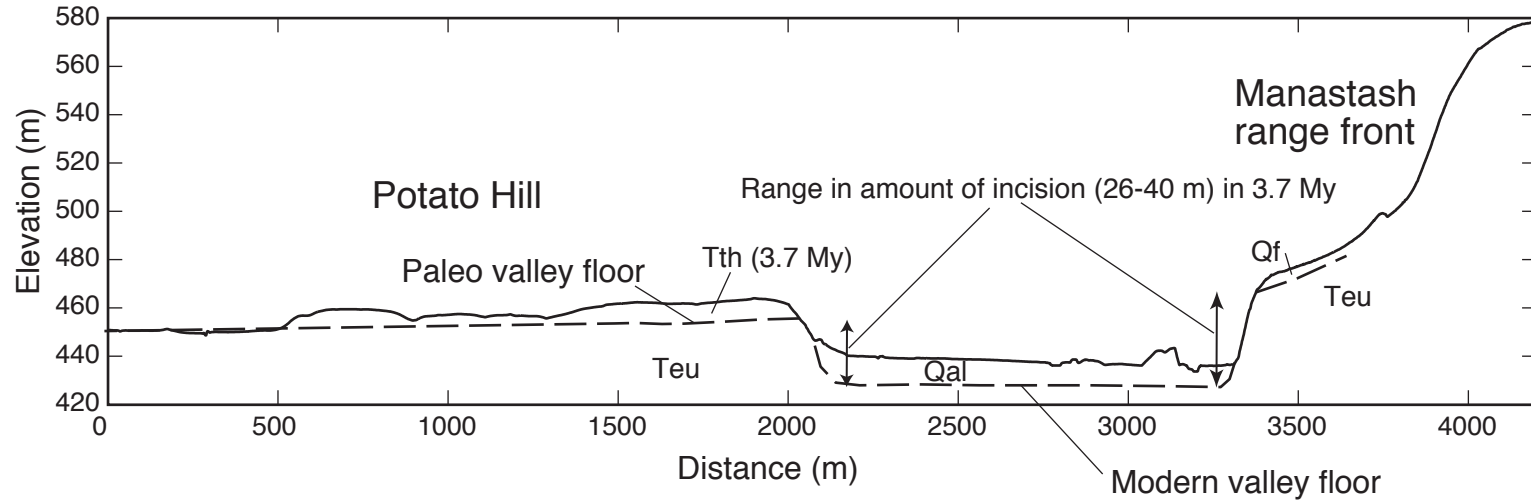


Figure 16. Cross section extending from Manastash range front northward to Potato Hill within the southern Kittitas Valley. Teu, Upper Ellensburg Formation; Tth, Thorp gravel of Waitt (1979); Qf, Quaternary fan deposit.

APPENDICES

Appendix A

October 30, 2011

Report from Shannon Mahan, USGS Luminescence Dating Lab, Denver CO

Report to Harvey Kelsey, Brian Sherrod, and Tyler Ladinsky

Please find enclosed a table of final ages and data for six samples from loess deposits mantling alluvial terraces along Manastash Ridge in the Kittitas Valley, Washington.

Key findings:

During sample preparation all samples showed a prolonged reaction to hydrogen peroxide treatments of 35%. This indicates large quantities of organic carbonates, usually formed during stabilization periods, with prolonged groundwater contact or wetting, or during soil formation. There was very little reaction to a 4N HCL treatment applied before the hydrogen peroxide and this tends to confirm the organic carbonate hypothesis.

The purified quartz extracts from all samples gave unsatisfactory data and dose response after being stimulated by blue light at 460 nm from a ring of diodes. The quartz was examined microscopically to see if there were impurities or inclusions, but all grains were a clear and even color. The quartz was not altered in any way and was not contaminated with plagioclase grains. However, no usable data could be obtained from the quartz OSL and this line of inquiry was discontinued. A sample curve of the quartz “decay curve” signal is included in this report (Figure 1, MN10-5). I speculate that the slow decay noted in these quartz separates corresponds to a volcanic source for the quartz and volcanic quartz is not noted for being amenable to OSL dating because it does not have a “fast” component signal (Preusser, et al 2010). For comparison, I have included a curves from AM10-2 and curves from another study that show the fast component response we are looking for (Figure 2a and Figure 2b). I have chosen a very similar response for both samples so that the height in the Y-axis is not considered a contributing factor to baseline level.

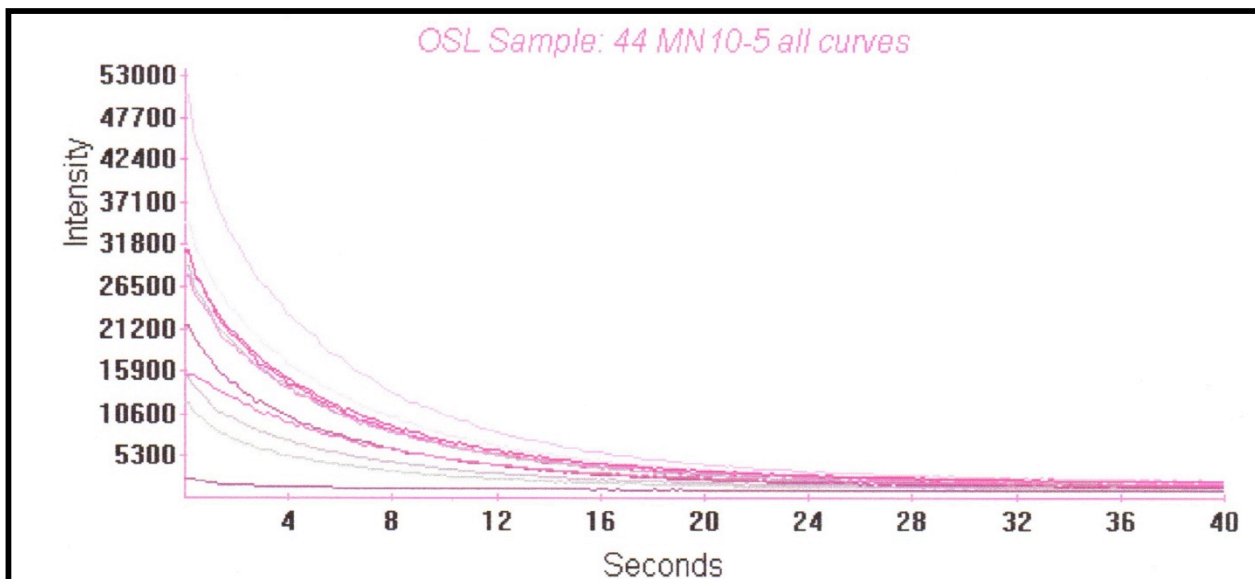


Figure 1: An OSL decay signal for sample MN10-5. The x-axis is in seconds of illumination (from 0 to 40 seconds) and the y-axis is in photonic intensity. This figure shows a mix of curves derived from the same sample of MN10-5. The lowest signal is from the “bleached” set of conditions and the highest intensity curve is from an exposure to a beta source of 400 Grays (4600 seconds). The natural curve lies somewhere around 16,000 photons. All samples show a middle or slow decay, only eventually coming to a zero count at around 30 seconds.

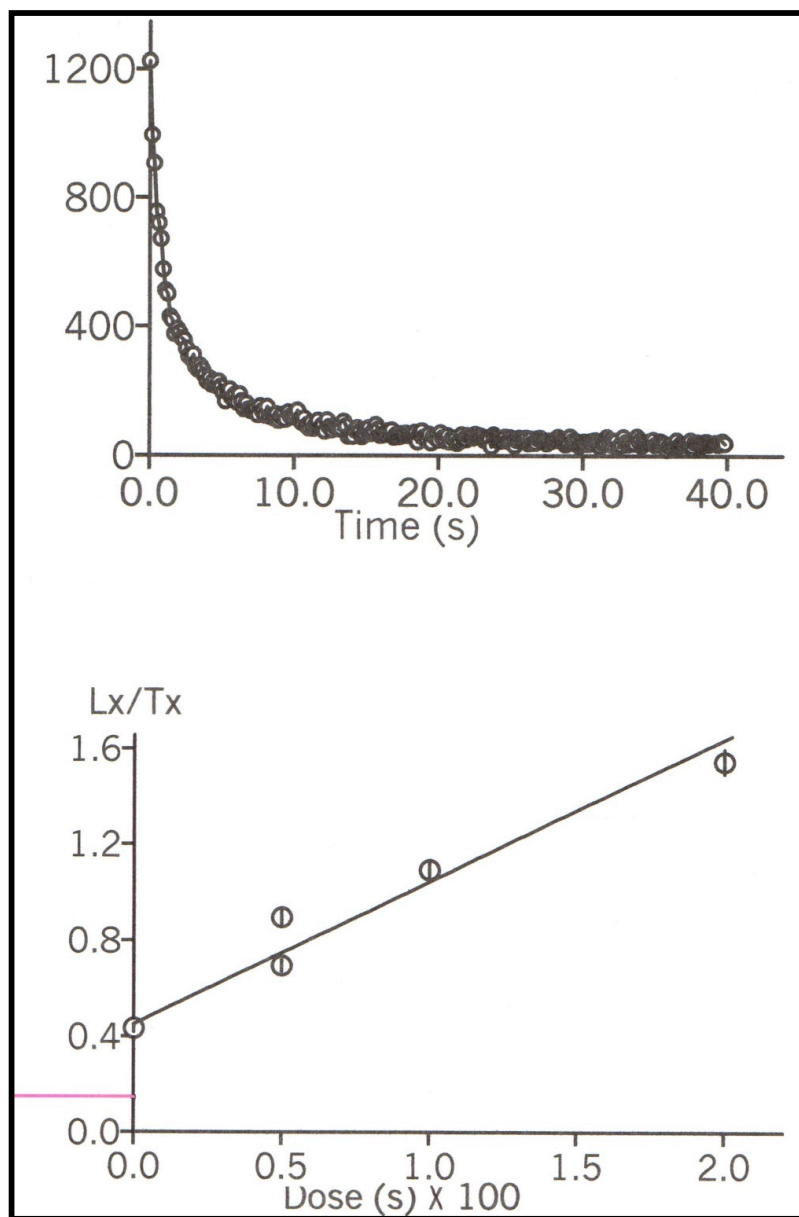


Figure 2a: OSL properties: (top) **OSL Decay Curve** for AM10-2 showing the quartz signal as stimulated with blue-light wavelength emitting diodes. Time is measured in seconds (s) and OSL is measured in photons counts for a total time of 40 seconds. Note the higher baseline shown by the sample, not coming to a zero baseline until 30 seconds. (Bottom) **OSL Growth Curve**, with the natural plotted on the L_x/T_x axis. Regeneration did not proceed “optimally” (recycle outside 10% of the first measurement shown by double circles above the 0.5 on the x-axis). The open circles show increases in response to increasing beta radiation. Fit is to a linear function but because of a thermal transfer problem, an equivalent dose cannot be tied to a zero. The “zero” is shown on the 0.4 of the y-axis, while the natural is the thin red line lower on the axis. Dose is measured in

Gray (absorbed radiation) and OSL is measured in unitless normalized OSL sensitivity measurements (L_x/T_x).

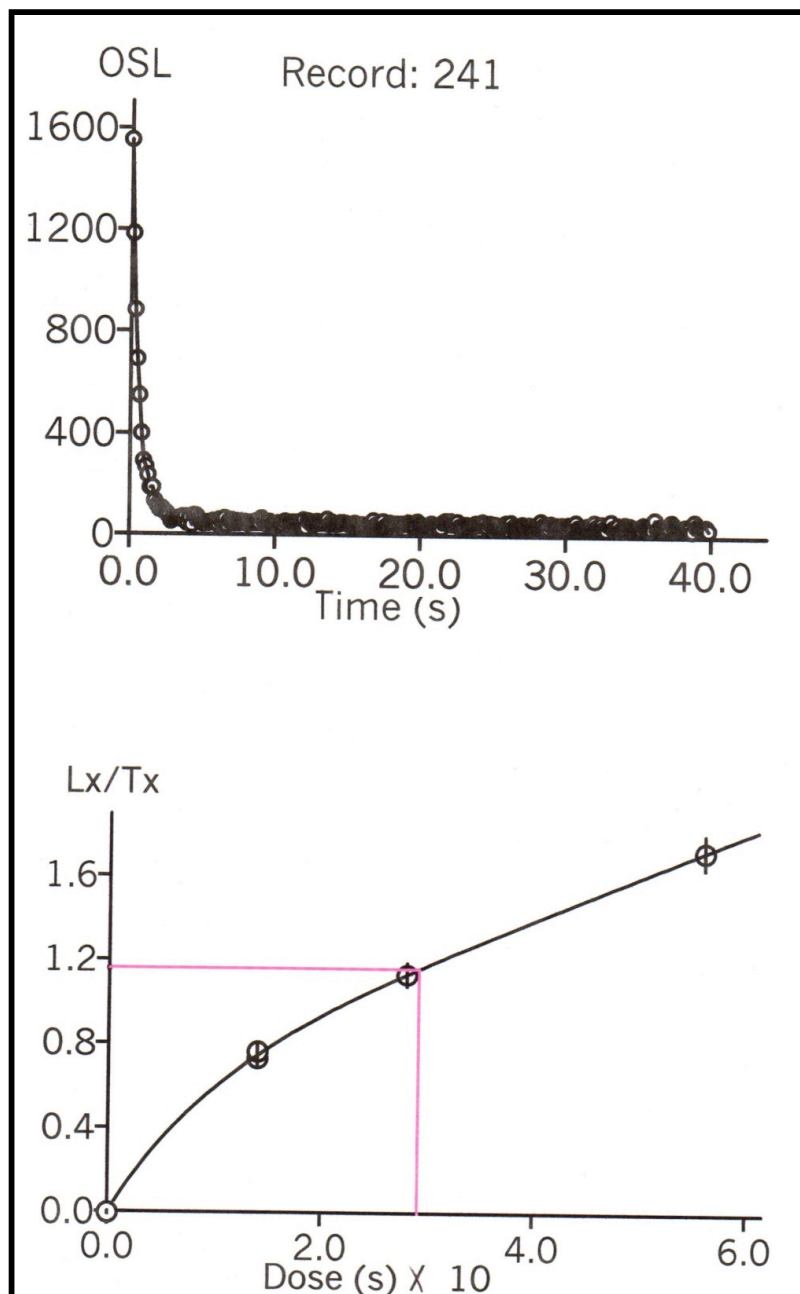


Figure 2b: OSL properties: (top) **OSL Decay Curve** for flood sample from the Black Hills, SD showing the quartz signal as measured with blue-light wavelength emitting diodes. Time is measured in seconds (s) and OSL is measured in photons counts for a total time of 40 seconds. Note that the sample immediately hits baseline after 5 seconds or less.

(Bottom) **OSL Growth Curve**, with the natural plotted on the L_x/T_x axis at 1.2. Regeneration proceeded “optimally” (recycle within 3% of the first measurement, shown by double circles above the 1.5 on the x-axis). The open circles show increases in response to increasing beta radiation. Fit is to an exponential + linear function. The zero is shown as an open circle at 0.0 on the y-axis and the natural intersects the fit at the red lines. Dose is measured in Gray (absorbed radiation) and OSL is measured in unitless normalized OSL sensitivity measurements (L_x/T_x).

Because the quartz was suboptimal, I turned my attention to the luminescence derived from the potassium feldspars (i.e. orthoclase, sanidine, microcline), probably dominantly from orthoclase. This luminescence is known as infrared stimulated luminescence (IRSL) because it is stimulates those feldspars with infrared diodes at 880 nm (Table 2). Initially, I thought the ages would be quite old (anywhere from 100,000 years to 500,000 years) and set laboratory templates up with this in mind. The first samples I measured were the two AM samples. AM10-1 returned an age of about 89,000 years, which seemed consistent with the brief outline and estimated age of the sample.

However, in very short order, AM10-2, MN10-1, MN10-2, MN10-3, and MN10-4 all returned about the very same ages; all around 40,000 to 48,000 years old. Sample MN10-5 returned an age of about 21,000 years. These 40,000 year old ages were quite puzzling, given that the age estimates were somewhere around 500,000 years, or at the very least expected to be older than about 100,000 years from field relationships, if I understood my e-mails correctly. The 40,000 years old ages seemed too coincidental, so I investigated three lines of research: *the luminescence saturation potential of the samples, the fine-grained (silt-sized) sediment diagnostics, and sample characteristics of the IRSL decay and growth curves.*

Luminescence saturation potential: The equivalent dose (D_e) values were all well below saturation values for infrared stimulated luminescence (IRSL). Clearly the equivalent dose could be pushed to as high as 1,380 Gys without reaching a saturation level (saturation level is defined as a straight line between radiation sets, not a rising line). As an example, Figures 3a and 3b show an IRSL decay and growth curve from AM10-1. (Please forgive the poor quality of the figures as well as the handwriting on them, it seemed more important to get my point across quickly without doing a bunch of drafting).

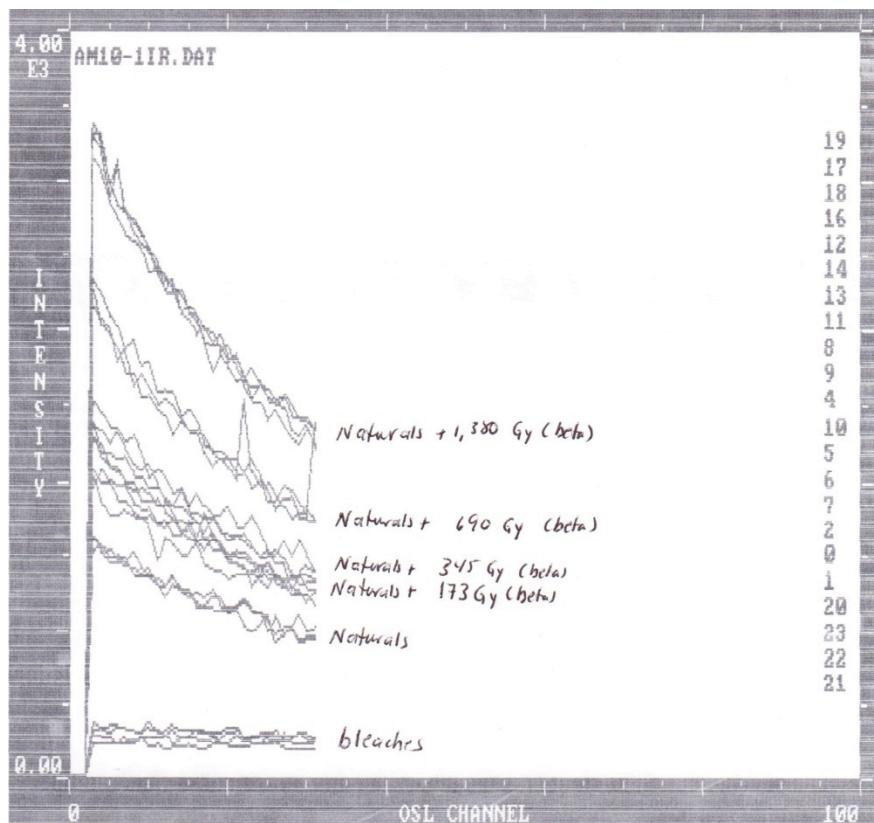


Figure 3a: IRSL properties: **IRSL Decay Curves** for AM10-1 showing the feldspar signal as a series of increasing intensity lines. The x-axis is the time counted in seconds and each OSL channel is one second. The y-axis is measured in photons counts or photonic intensity. Note that although the sample does not ever hit a baseline, this is perfectly natural in IRSL and does not raise alarm.

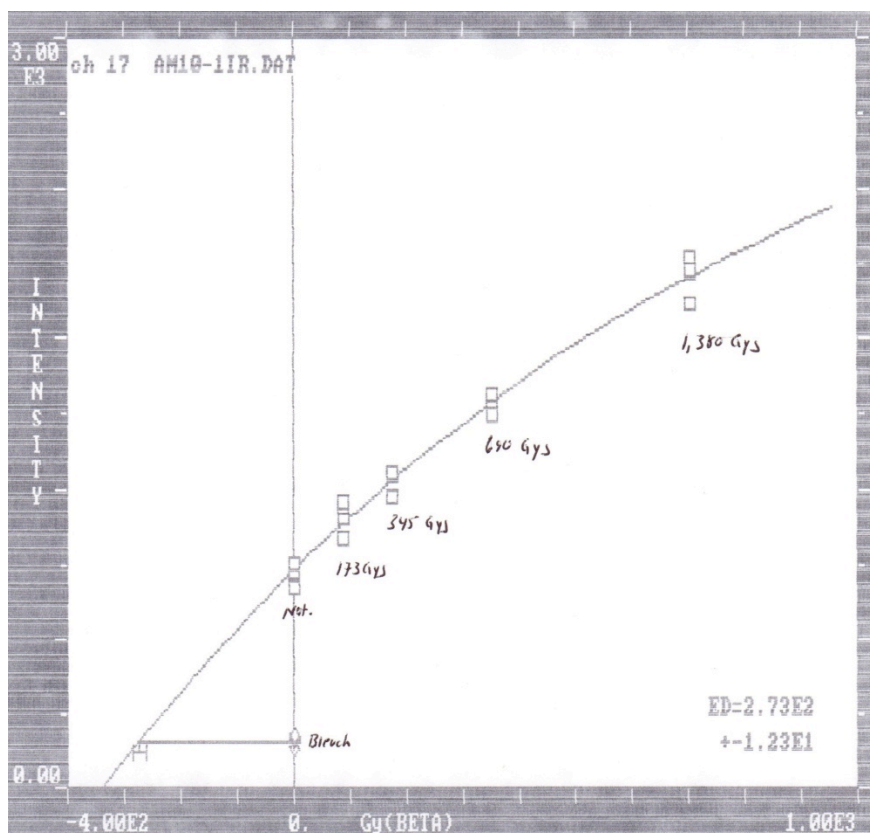


Figure 3b: OSL properties: **IRSL Growth Curves** for AM10-1 showing the feldspar signal as it is added to in intensity by exposing the grains to a beta source of known radiation (Grays or Gy). The x-axis is the measured equivalent dose (here shown as ED, I speak in the report of De, they are the same thing) when compared to calibrated Grays generated by exposure to a beta source. The y-axis is measured in photons counts or photonic intensity. Note that the sample radiation intensity continues to rise unchecked or unflattened by a saturation response.

So why did the four samples listed previously return ages that are all fortuitously about 40,000 years old? Are these ages real? Given the fact that none of the IRSL curves ever reached saturation, even when pushed, tells me that the issue is very unlikely to be an underestimate resulting from extreme sample saturation that occurred in the last depositional phase of the naturals (i.e. the sample sediment did not sit around long enough to fill all the electron traps with luminescence). The samples would have to be about 460,000 years old to get to a 1,380 Gy level (assuming a dose rate of 3 Gys/ka), so clearly even if the samples were “old” I should have been able to decipher that (Figure 4 does show MN10-3 in saturation). Therefore I do not think the problem is any sort of saturation whether natural or lab induced, *unless the samples are significantly older than 400,000 to 500,000 years old.*

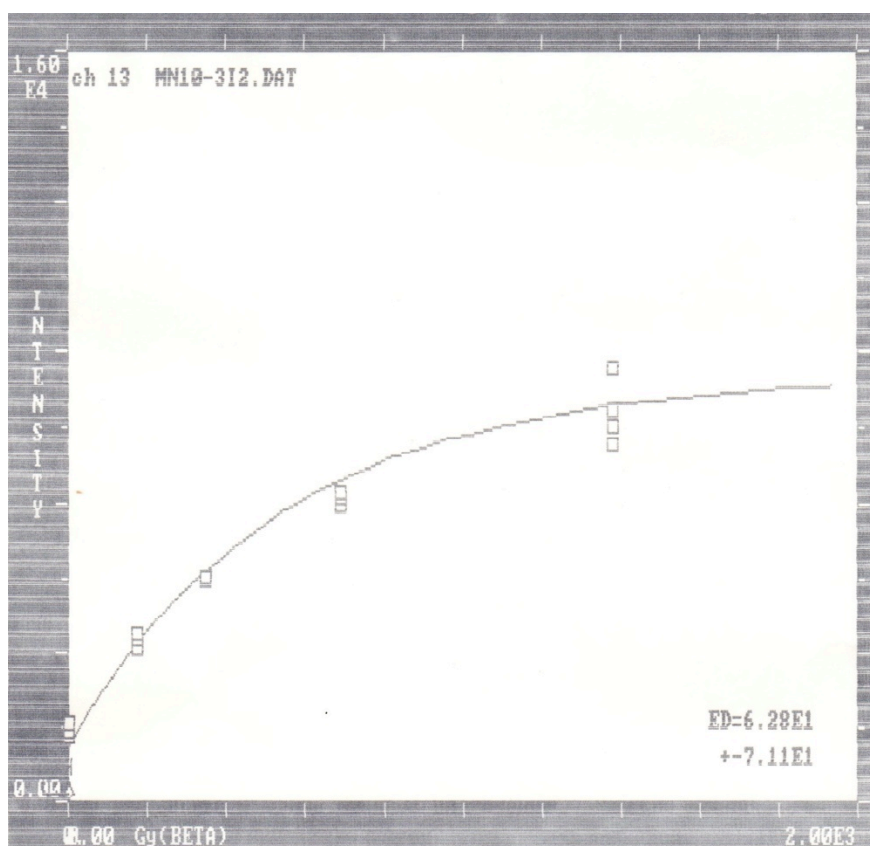


Figure 4: OSL properties: **IRSL Growth Curves** for MN10-3 showing the feldspar signal as it is added to in intensity by exposing the grains to a beta source of known radiation (Grays or Gy). The x-axis is the measured equivalent dose (here shown as ED, I speak in the report of De, they are the same thing). The y-axis is measured in photons counts or photonic intensity. Note that the sample radiation intensity begins to flatten out between the third and fourth irradiation sets. This is saturation.

Fine-grained (silt-sized) sediment diagnostics: Microscopic analyses were conducted on cleaned AM10-1 grains (after HCl, hydrogen peroxide and sieving). This sample had lithic grains that were dark in nature and did not crush easily between tweezers or forceps. I guessed these were basalt sourced lithics and composed about 20-25% of the sample. Both the AM samples showed these dark lithic grains while the MN samples did not. The feldspar grains look fresh and unaltered and there are minor amounts of quartz and potassium feldspars, but major amounts of plagioclase.

Microscopic analyses were conducted on cleaned MN10-1 grains. This sample had shards that were easily broken apart and looked “glassy”, possibly a tephra influx or possible inexperience on the part of the examiner at looking at silt loess composition from eastern WA (is it just finely ground quartz?). There are minor amounts of quartz

and potassium feldspars but major amounts of plagioclase. The K-spar grains looked like they have tiny surface pitting in them but are otherwise unaltered.

In my earlier e-mails to Harvey I reported “horribly altered” feldspars. These turned out to just be the silt and clay coatings that caked most grains. Once these were adequately cleaned off (i.e. acid treatments and not water) the grains themselves could be studied instead of the coatings. Also, although AM10-2 is noted as coming from an alluvial sand instead of a loess, all the elemental concentrations of K, U, and Th were consistent, again indicating that everything is sourced from the same geology. There should be no difference to the luminescence measurements of such samples.

The sample characteristics of the IRSL decay and growth curves: The IRSL decay and growth curves all showed the same response to laboratory induced irradiation (i.e. artificially aged in the lab) and did not reach saturation even after exposure to 600 Gy or 700 Gy or 1,380 Gy (for the most part). I used the methodology considered to be the classic fine-grained technique, namely the multiple aliquot additive dose (Richardson et al, 1997). Usually this technique returns ages that are *too old* as it does not adequately address problem of partial bleaching of samples. I figured partial bleaching (or partial erasure of previously generated luminescence at the last depositional setting before the depositional setting of interest or sampling) was not as significant a problem as would be the saturation problem. I also used the more dominant mode of the loess, the silt-sized grains instead of the fine-sand sized grains to date the sample.

One more avenue that I felt must be explored was to test the rate of anomalous fading in the K-spars (an observation that the field saturation luminescence intensity is less than the laboratory saturation intensity in feldspars due to electron “tunneling” from principal luminescence traps to nearby structural defects in the sediment mineral). Every feldspar or feldspar extract from sediments that has been analyzed in detail (Huntley and Lian, 2005) shows measurable tunneling or anomalous fading. For plagioclase feldspars there is a strong tendency for the fading rate to increase with increasing Ca and/or Fe content and this is the primary reason why they are not used for IRSL dating. No generalization can be made like this for alkali feldspars. I could not find in either Kate Richardson paper (1997) or Glenn Berger’s paper (1995) where they had measured anomalous fading ratios on their TL and IRSL ages. They may have, and in Glenn’s case we may never know since he died earlier this year, but not reported them or put them in an appendix.

Because each sample needs to be tested, the process is a bit laborious (thus the loooong wait until you hear from me after each set of questions). Samples AM10-1 and MN10-5 showed a slight fade of about 2-3%. However, because the fit to the radiation sets was not linear but exponential for much of the fit, it is not recommended to adjust any sample over about 20,000 years old using the accepted equations (Huntley and Lamothe, 2001). So I did not. I reported the ages without correction. The fading rates were small anyway

and unlikely to correct the ages with any real meaning outside the current errors associated with ages.

In the meantime I read a very interesting paper by Mortheikai et al, 2011 (complete reference below). They took eight samples from basalt flows in the Azores (Portugal) that corresponded in age ranges from 400 ka to 2.2 Ma. Two of the youngest flows were dated by other means at about 400 ka. They returned IRSL ages of 23 ka and 85 ka...eerily similar to my package of 40 ka ages! These are huge underestimates. By applying a set of parameters that I admit are not easily decipherable by me, let alone other OSL scientists, the authors were able to adjust the ages of the 400 ka basalt flows to 305 ka and 324 ka, with larger errors (typically more than 10%, sometimes as much as 35%). Their decay curves also did not show saturation until well into the 2000 and 4000 Gray category, something I never got to, mainly in the interest of time, since this would require considerable exposure to my beta source and create a sample logjam in the lab.

Reading further through paper I noticed that a common denominator was about a 13% fading rate (per unit of decade time). When I measured the fading rates on MN10-2, MN10-3, and MN10-4 I got fading rates anywhere from 11% to 18%. AM10-2 had fading rates that were lower, around 8%. If I average every fading rate I got from the four samples I come up with about a 12% fading rate, so the 13% seems a good estimate. Because I would like to hold the correction rate to a constant until I know more about the individual workings of the mineralogy I put an additional line in the table below each of the four samples with the corrected age given a 13% fade rate. Now I know the calculations probably seem like a bit of mumbo-jumbo and my explanation is equally hopelessly complicated and obtuse, *so I would like you to treat these four corrected ages as minimum ages. In other words, the true age is probably greater than the corrected IRSL ages.*

So, what is my final conclusion? The luminescence data tells me that the ages for AM10-1 and MN10-5 are likely to be reasonable and unaffected to a large degree by anomalous fading. The luminescence data also tells me that if the sample is old enough (i.e. >400 ka) then the processes of anomalous fading in both the field and laboratory settings have strongly influenced the measured age of the sample. Until more detailed and reproducible results have been generated I cannot give any reliable ages for old loess samples in eastern Washington. I suspect this is why not too many ages older than 100,000 years have been reported as researchers have either run into a large and complicated anomalous fading problem or they simply stayed away from sampling anything older than 100,000 years.

Ways to test these assumptions: 1). Bring back a sample of known age that is older than 100,000 years for me to run tests on. I would be quite keen to see if my anomalous fading results hold up in "reality". 2). If the samples are really 40,000 years old are there any associated tephras such as Tephra Set C (Ape Canyon Stage 36-50 ka)? 3). If the

samples are in excess of 300,000 years old, as the corrected ages would indicate, are there associated tephras that would confirm this? 4). Is the loess recycled such that intact grains and carbonate nodules are simply swept from one location to another, and older loess deposits actually source younger loess deposits, complicating the anomalous fading histories? The answer lies in looking at both rock source and material derived from the source using IRSL.

TABLE 1: IRSL (K-Feldspar) Data and Ages from Manastash anticline, Eastern WA

Sample information	% Water content ^a	K (%) ^b	U (ppm) ^b	Th (ppm) ^b	Cosmic dose ^c additions (Gy/ka)	Total Dose Rate (Gy/ka)	Equivalent Dose (Gy)	Age (yrs) ^d
AM10-1	4 (37)	1.00 ± 0.03	1.67 ± 0.08	4.87 ± 0.25	0.20 ± 0.02	2.65 ± 0.08	235 ± 10.6	88,750 ± 4,520
AM10-2	6 (46)	1.10 ± 0.03	1.23 ± 0.07	3.23 ± 0.24	0.20 ± 0.02	2.27 ± 0.09	102 ± 5.54 fade corrected	45,000 ± 2,990 254,250 ± 17,080
MN10-1	8 (43)	0.82 ± 0.03	1.19 ± 0.08	5.47 ± 0.29	0.17 ± 0.01	2.25 ± 0.08	108 ± 11.3 fade corrected	47,890 ± 5,340 279,020 ± 31,240
MN10-3	5 (53)	0.88 ± 0.02	1.33 ± 0.06	4.86 ± 0.22	0.17 ± 0.01	2.24 ± 0.06	93.7 ± 3.94 fade corrected	41,810 ± 2,140 228,220 ± 11,900
MN10-4	7 (55)	0.87 ± 0.03	1.50 ± 0.07	5.30 ± 0.27	0.17 ± 0.01	2.34 ± 0.08	94.3 ± 3.03 fade corrected	40,240 ± 1,880 215,880 ± 10,310
MN10-5	2 (35)	1.42 ± 0.03	1.62 ± 0.06	4.07 ± 0.26	0.18 ± 0.01	2.91 ± 0.09	60.7 ± 3.96	20,860 ± 1,520

^aField moisture, figures in parentheses indicate complete saturation %. Ages calculated using about 25% saturation for all samples.

^bAnalyses obtained using laboratory Gamma Spectrometry (high resolution Ge detector) and readings are delayed after 21 days of being sealed in the planchet (used for dose rates).

^cCosmic doses and attenuation with depth were calculated using the methods of Prescott and Hutton (1994).

^dDose rate and age for IRSL from fine-grains of 4-11 micron polymineral silt. Exponential fit used for equivalent dose, multiple aliquot additive dose. Errors to one sigma.

Fade tests indicate a g value of 1 or 2%/decade for AM10-1 and MN10-5. For AM10-2, MN10-2, MN10-3, and MN10-4 the g value is 13.2%/decade.

TABLE 2: Luminescence parameters used in preparation and analyses of samples for IRSL

Measurement parameters:

Machine Daybreak 1100 Luminescence Reader

Mineral; grain size: polymineral: 4-11 μ m

Stimulation source: 20 IR diodes, emission centered on 880 nm

Power delivered to aliquot: 100 mW/cm² (full strength)

Duration of stimulation: 30 seconds

Final signal level: 10% of initial

Photomultiplier: EMI 9235QA quartz window bialkali

Aliquot temperature: 30 °C

Detection filters: Schott BG-39 + Corning 7-59 (blue)

Normalization: natural (0.5 sec at reduced voltage)

Preheat: 124 °C for 64 hours

Delay before measurement: 24 hr or more

Equivalent dose evaluation: additive method using integrated OSL/ satisfactory plateau for TL

Background evaluation: after bleaching with natural sunlight and quartz window

Alpha effectiveness: fine grains: $a = 0.06-0.08$

Dose-rate evaluation: lab gamma spectrometer (high- resolution Ge)

Dose rate range: 2.24-2.91 Gy/ka (unusually narrow, indicating same source for all loess)

Water content: 2-8% field and 35-55% saturated

Cosmic-ray contribution: 6-9% of total dose rate

Table 3: Multiple Aliquot Additive Dose Procedure.

1. Beta irradiation of sets of discs (4 in a set), doubling the dose for each successive set. Second set is kept close to expected dose from the natural
2. Bleaching of a set of discs for 8 hours (or longer) by exposure to natural sunlight
3. 24 hour delay
4. All discs, including set of naturals, put into preheat 124 °C for 64 hours
5. 24 hour delay
6. Stimulation with infrared diodes and data collection

References in report:

- Berger, G.W. and Busacca, A.J., 1995. Thermoluminescence dating of late Pleistocene loess and tephra from eastern Washington and southern Oregon and implications for the eruptive history of Mount St Helens. *Journal of Geophysical Research* **100** 22361–22374.
- Huntley DJ and Lamothe M, 2001. Ubiquity of anomalous fading in K-feldspars and the measurement and correction for it in optical dating. *Canadian Journal of Earth Sciences* 38(7): 1093-1106, DOI [10.1139/e01-013](https://doi.org/10.1139/e01-013).
- Huntley D.J. and Lian, O., 2005. Some observations on tunneling of trapped electrons in feldspars and their implications for optical dating. *Quaternary Science Reviews* 25 (19-20), 2503-2512.
- Morthekai, P., Jain, M., Cunha, P. P., Azevedo, J.M., and Singhvi, A.S., 2011. An attempt to correct for fading in million year old basaltic rocks. *Geochronometria* 38(3), 223-230.
- Preusser F, Chithambo M.L., Gotte T, Martini M, Ramseyer K, et al. 2009. Quartz as a natural luminescence dosimeter. *Earth-Sci. Rev.* 97, 184–214.
- Richardson, C.A., McDonald, E.V. and Busacca, A.J. (1997). Luminescence dating of loess from the northwest United States: *Quaternary Science Reviews*, v. 16 (3-4), 403-415.

Appendix B

USGS Tephrochronology Project Report: TL100110-1 Manastash Ridge
Anticline/Yakima Fold Belt area, WA

Received from Elmira Wan March 31, 2011

Here is the tephrochronology report on TL100110-1, your sample from between Spring Canyon and Dead Cow Gulch (Manastash Anticline/Yakima Fold Belt area) in Kittitas Valley, Washington.

Using electron microprobe, we analyzed for nine major and minor oxides (SiO₂, Al₂O₃, FeO, MgO, MnO, CaO, TiO₂, Na₂O, K₂O). The raw data were then recalculated to a 100% fluid-free basis. Next, similarity coefficient analyses were performed on the chemical data, and the normalized values compared to geochemical “fingerprints” (currently ~5,900) in our reference database. For a complete tephrochronologic interpretation of the submitted samples, independent age control, stratigraphic positions, field and petrographic characteristics, and mineralogy were also considered. Holly Olson did the sample processing and descriptions, Dave Wahl performed the microprobe and computer analyses, and I interpreted the data. The raw and normalized chemical data, comparative chemical data, and lists of chemical correlatives are in the attached MS-Excel and Word files.

TL100110-1: Correlates well (≥ 0.94 similarity coefficient, with and without alkalis) to late Pleistocene tephra layers derived from Mount Saint Helens eruptions. (See highlighted samples in MS-Word file: rec TL100110-1 T582-10.doc.)

With alkalis, the best chemical match (> 0.95 SC) is to sample #3 St Helens Yn (gray highlight), although the iron is a bit lower in TL100110-1. Clynne and others (2008) report an age range of 3,900-3,300 yr B.P. for Mount Saint Helens set Y tephra. If you look at page one in MS-Word file: rec TL100110-1 T582-10.doc, you will see other good correlations to Mt. St. Helens Set Y (Ye and Yn) tephra (also in gray highlight), as well as to other, and older (~100 ka – 41 ka) sets of tephra from this volcanic source (yellow, and green highlighted samples, respectively).

Along this note, without alkalis, and with 0.976 and ~0.96 SCs, TL100110-1 most closely matches CL-90A [(2) and -(1)], multiple analyses of a 7-cm thick ash bed at 19.80 to 19.73 m, depth, in a sediment core recovered from Carp Lake in Washington (yellow highlight). The collector was Cathy Whitlock who is now at Montana State University at Bozeman. Your sample also matches very well with CARP-10, another Whitlock sample which is a ~40-cm-thick ash layer immediately above CL-90A, at 19.50 to 19.11 m in the core. The iron and calcium levels are more comparable between these ash beds and

TL100110-1 then with the MSH Set Y samples. WA 5-19 is another good correlative (0.956, SC). Alan Busacca (Washington State Univ.) collected this sample from an unnamed Mount Saint Helens tephra layer in the Palouse Fm near Washtucna, WA. He describes WA 5-19 in Busacca and others, 1992 (QR 37, p. 281-303). When this sample was submitted back in 1986, Alan Busacca suggested that it was probably somewhere between 150-75 ka, based on the presence of two Mount St. Helens C-like ash beds above, and a soil that intervened between WA5-19 and the two MSH C-like layers. In the QR article, he limits the age to about 100 - 60 ka. Whitlock and others (2000) also correlate CARP-10, CL-90A (2) and CL-90A (1) to WA 5-19. These authors report an uncalibrated ¹⁴C age of ~100 ka for the Carp Lake samples, and in turn, for WA 5-19.

It should be noted that a couple of chemical correlations to Mount Saint Helens layer Cy (sample I.D.s: GS-54M and CYSH2, green highlight) appear in the recalculated data table. However, the comparatively low calcium levels in the MSH Set C samples, and the considerably hydrated condition of TL100110-1 (93.723 total wt. %, see Excel file: TL100110-1 T582-10.xls) suggest that while your sample exhibits some chemical similarities to MSH Cy tephra, it probably is not derived from this eruption but from an earlier Pleistocene eruption given the poor to moderate preservation of the glass shards. The Carp Lake tephra are similarly leached and highly hydrated; their totals average 93.0%. Mount St. Helens Ye and Yn total 98.9% and 99.4%, respectively. Further, in the Carp Lake core, the candidate correlatives, CL-90A [(1) and (2)] and CARP-10, are overlain by three Mount St. Helens C-like ash layers. In the Carp Lake core, two thin ash layers at 19.07 to 19.06 m and 18.64 to 18.57 m, CARP-9 and CARP-8, respectively, are also Mount St. Helens C-like in chemical composition. However, these tephra obviously are quite a bit older as they 1) proximally overlie CARP-10 and CL-90A, and 2) underlie by 9-10 m, CARP-5, a definitively identified, 50,000-35,000 yr B.P. (uncalibrated) MSH set C ash bed. Given the geochemical and stratigraphic evidence, it seems reasonable to assume that TL100110-1 most likely correlates to the ~100 ka set of late Pleistocene tephra layers.

In closing, I hope that the tephrochronologic results provide a chronologic framework and fit well within the stratigraphic context of your study of the Manastash Anticline and Yakima Fold Belt area. I look forward to hearing your thoughts on these results, and hope we can further collaborate on this investigation in the future.

If you have any questions regarding our results, please feel free to write or call me. My contact information follows below.

Best regards,

Elmira Wan
Tephrochronology Project
U.S. Geological Survey

Listing of 37 closest matches for COMP. NO. 5884 for elements: **Na, Mg, Al, Si, K, Ca, Ti, Fe** Date of Update: 3/28/11

C.No	Sample Number	Date	SiO2	Al2O3	Fe2O3
MgO	MnO	CaO	TiO2	Na2O	K2O Total, R Sim. Co

1	5884 TL100110-1 T582-10	2/16/11	77.19	14.24	1.18
0.35	0.04	1.81	0.13	2.98	2.07 99.99 1.0000
2	808 GS-54M		77.52	14.32	1.17
0.34	0.03	1.67	0.13	2.60	2.20 99.98 0.9611 Correl. MSH Cy = 47±2 ka, TL
3	3074 ST HELENS Yn T5-4	8/5/93	75.67	14.83	1.29
0.36	0.04	1.80	0.13	3.78	2.09 99.99 0.9501 MSH Set Y 3,900-3,300 yr B.P.
4	2800 CL-90A (2) T255-3	4/14/92	75.38	14.51	1.29
0.35	0.06	1.84	0.13	4.19	2.25 100.00 0.9359 Palouse Fm., Washtucna=CARP-10
5	428 YeSH, T5-3		75.65	14.52	1.32
0.34	0.03	1.68	0.13	4.26	2.06 99.99 0.9311 MSH Layer Ye 3.69 ka, cal.
6	3521 ah95-8k kaufman		77.14	14.36	1.26
0.34	0.05	1.76	0.11	2.58	2.40 100.00 0.9307
7	2674 TLWM-2.5 T240-6	9/28/91	76.77	13.54	1.30
0.35	0.04	1.72	0.14	3.98	2.16 100.00 0.9299
8	3071 CARP-2 MAJ T281-3	8/5/93	75.98	14.32	1.25
0.34	0.04	1.65	0.14	4.15	2.13 100.00 0.9280 = MSH Layer Ye 3.69 ka, cal
9	3520 ah95-3p		77.01	14.51	1.23
0.34	0.05	1.84	0.10	2.58	2.34 100.00 0.9266
10	3073 ST HELENS Ye T5-3	8/5/93	76.12	14.40	1.25
0.34	0.05	1.72	0.16	3.85	2.11 100.00 0.9260 MSH Layer Ye 3.69 ka, cal.
11	2357 TWN-L-1.445		76.35	14.14	1.21
0.34	0.00	1.69	0.16	3.98	2.12 99.99 0.9250
12	3016 CARP-10 T279-5	5/26/93	75.43	14.38	1.20
0.38	0.04	1.81	0.12	4.39	2.24 99.99 0.9247 CARP Lake Ash 10, ~100 ka, ¹⁴ C
13	3688 MCB 65 T340-4	11/96	75.86	14.10	1.37
0.38	0.04	1.75	0.13	4.20	2.17 100.00 0.9232
14	3771 942-93		77.10	14.36	1.50
0.37	0.05	1.86	0.15	2.77	1.84 100.00 0.9227
15	1558 WA 5-19	7/18/86	76.24	13.61	1.25
0.36	0.06	1.90	0.12	4.26	2.20 100.00 0.9220 Palouse Fm., Washtucna=CARP-10

16	2799	CL-90A (1)	T255-3			4/14/92	75.53	14.51	1.21
0.34	0.05	1.82	0.11	4.14	2.29	100.00	0.9214	Palouse	
Fm., Washtucna=CARP-10									
17	430	YnSH,	T5-4				74.99	14.90	1.34
0.34	0.04	1.79	0.14	4.39	2.06	99.99	0.9213	MSH Set Y	3,900-
3,300 yr B.P.									
18	3686	EFWR	53 T340-1			11/96	76.16	13.96	1.24
0.35	0.04	1.66	0.15	4.29	2.15	100.00	0.9200		
19	3701	VWB	105 T341-4			11/96	75.86	14.21	1.36
0.36	0.04	1.70	0.14	4.12	2.20	99.99	0.9191		
20	3694	PLB	45 T340-8			11/96	75.70	14.17	1.34
0.34	0.03	1.75	0.14	4.33	2.20	100.00	0.9190		
21	3774	942-209	major				77.12	14.59	1.48
0.39	0.06	1.87	0.13	2.71	1.65	100.00	0.9180		
22	3278	93P52	T308-3			8/1/94	75.29	14.60	1.28
0.36	0.04	1.83	0.15	4.19	2.26	100.00	0.9160		
23	3986	SKY-V-2	T364-5			5/97	76.34	13.98	1.19
0.28	0.03	1.62	0.13	4.22	2.21	100.00	0.9125		
24	429	Yn-7-15-72-8,	T3,4				75.54	14.23	1.40
0.37	0.08	1.81	0.15	4.27	2.14	99.99	0.9123	MSH Set Y	3,900-
3,300 yr B.P.									
25	4922	PLW8/11/01P1_POP1	T483-8			10-26-02	76.14	14.37	1.07
0.35	0.02	1.82	0.09	4.03	2.10	99.99	0.9120		
26	3702	VWB	105 #2 T341-4			11/96	76.10	14.04	1.29
0.35	0.05	1.66	0.15	4.22	2.26	100.12	0.9116		
27	4938	PLW8/11/01_P3	T487-4			10-26-02	76.55	14.19	1.02
0.34	0.04	1.79	0.09	3.90	2.07	99.99	0.9087		
28	3765	WA-5-C	T349-4			11/96	75.51	14.63	1.11
0.32	0.06	1.72	0.14	4.09	2.42	100.00	0.9087		
29	228	MOD-4,	T12-9				73.66	16.09	1.30
0.35	0.06	1.80	0.13	3.71	2.90	100.00	0.9073		
30	4392	CYSH2	T401-8			12-3-98	76.23	13.88	1.11
0.34	0.04	1.66	0.15	4.26	2.32	99.99	0.9062		
31	4435	FL7.74-7.76M_POP1	T408-2			5-30-99	75.94	14.17	1.16
0.32	0.05	1.77	0.17	4.12	2.32	100.02	0.9043		
32	4647	RAFT4673,	T405-10			04/01/00	75.14	14.46	1.35
0.38	0.04	1.92	0.14	4.22	2.35	100.00	0.9015		
33	5618	JEO 7/27/06-1(1)	T561-10			4/28/08	76.16	14.46	1.43
0.35	0.05	1.72	0.20	3.48	2.16	100.01	0.9014		
34	1513	MOD-4 (2) (373)	T119-14			4/28/86	74.85	14.90	1.26
0.39	0.12	1.86	0.12	3.59	2.90	99.99	0.8999		
35	3985	SKY-V-1	T364-4			5/97	76.40	13.91	1.17
0.29	0.04	1.65	0.15	4.13	2.27	100.01	0.8998		
36	3952	95T0-B260B	T360-2			4/97	76.72	13.48	1.18
0.31	0.05	1.59	0.14	3.83	2.70	100.00	0.8973		

37 2958 RFUA-MFT-AV 76.85 13.32 1.21
 0.37 0.00 1.60 0.15 4.00 2.50 100.00 0.8970

Listing of 37 closest matches for COMP. NO. 5884 for elements: **Mg, Al, Si, Ca, Ti, Fe** Date of Update: 3/28/11

C.No	Sample Number	Date	SiO2	Al2O3	Fe2O3	
MgO	MnO	CaO	TiO2	Na2O	K2O Total,R	Sim. Co
1	5884 TL100110-1 T582-10	2/16/11	77.19	14.24	1.18	
0.35	0.04	1.81	0.13	2.98	2.07	99.99 1.0000
2	808 GS-54M		77.52	14.32	1.17	
0.34	0.03	1.67	0.13	2.60	2.20	99.98 0.9793 Correl. MSH Cy = 47±2 ka, TL
3	2800 CL-90A (2) T255-3	4/14/92	75.38	14.51	1.29	
0.35	0.06	1.84	0.13	4.19	2.25	100.00 0.9761 Palouse Fm,Washtucna =CARP-10
4	3074 ST HELENS Yn T5-4	8/5/93	75.67	14.83	1.29	
0.36	0.04	1.80	0.13	3.78	2.09	99.99 0.9703 MSH Set Y 3,900-3,300 yr B.P.
5	3016 CARP-10 T279-5	5/26/93	75.43	14.38	1.20	
0.38	0.04	1.81	0.12	4.39	2.24	99.99 0.9658 CARP LAKE ASH 10, ~100 ka, ¹⁴ C
6	428 YeSH, T5-3		75.65	14.52	1.32	
0.34	0.03	1.68	0.13	4.26	2.06	99.99 0.9591 MSH Layer Ye 3.69 ka, cal.
7	2799 CL-90A (1) T255-3	4/14/92	75.53	14.51	1.21	
0.34	0.05	1.82	0.11	4.14	2.29	100.00 0.9579 Palouse Fm,Washtucna =CARP-10
8	228 MOD-4, T12-9		73.66	16.09	1.30	
0.35	0.06	1.80	0.13	3.71	2.90	100.00 0.9569 Modelo Fm
9	1558 WA 5-19	7/18/86	76.24	13.61	1.25	
0.36	0.06	1.90	0.12	4.26	2.20	100.00 0.9559 Palouse Fm,Washtucna =CARP-10
10	3071 CARP-2 MAJ T281-3	8/5/93	75.98	14.32	1.25	
0.34	0.04	1.65	0.14	4.15	2.13	100.00 0.9557 = MSH Layer Ye 3.69 ka, cal
11	2674 TLWM-2.5 T240-6	9/28/91	76.77	13.54	1.30	
0.35	0.04	1.72	0.14	3.98	2.16	100.00 0.9553 Twin Lakes Wallowa Mtns
12	3694 PLB 45 T340-8	11/96	75.70	14.17	1.34	
0.34	0.03	1.75	0.14	4.33	2.20	100.00 0.9539 Poison Lake, ID

13	3688	MCB 65	T340-4			11/96	75.86	14.10	1.37
0.38	0.04	1.75	0.13	4.20	2.17	100.00	0.9537	Pinedale Moraine, McCall, ID	
14	3521	ah95-8k	kaufman				77.14	14.36	1.26
0.34	0.05	1.76	0.11	2.58	2.40	100.00	0.9529	Correl. CARP-10, CL-90A (1)	
15	3686	EFWR 53	T340-1			11/96	76.16	13.96	1.24
0.35	0.04	1.66	0.15	4.29	2.15	100.00	0.9504	Weiser River, Idaho	
16	3278	93P52	T308-3			8/1/94	75.29	14.60	1.28
0.36	0.04	1.83	0.15	4.19	2.26	100.00	0.9501	Correl. CARP-10, CL-90A (1)	
17	430	YnSH,	T5-4				74.99	14.90	1.34
0.34	0.04	1.79	0.14	4.39	2.06	99.99	0.9495	MSH Set Y 3,900- 3,300 yr B.P.	
18	3701	VWB 105	T341-4			11/96	75.86	14.21	1.36
0.36	0.04	1.70	0.14	4.12	2.20	99.99	0.9481	Van Wyck Creek Bog, Idaho	
19	3765	WA-5-C	T349-4			11/96	75.51	14.63	1.11
0.32	0.06	1.72	0.14	4.09	2.42	100.00	0.9476	Palouse Fm, Washtucna =CARP-10	
20	2357	TWN-L-1.445					76.35	14.14	1.21
0.34	0.00	1.69	0.16	3.98	2.12	99.99	0.9458	Twin Lakes Wallowa Mtns	
21	3702	VWB 105 #2	T341-4			11/96	76.10	14.04	1.29
0.35	0.05	1.66	0.15	4.22	2.26	100.12	0.9451	Van Wyck Bog	
22	3520	ah95-3p					77.01	14.51	1.23
0.34	0.05	1.84	0.10	2.58	2.34	100.00	0.9438	Correl. CARP-10, CL-90A (1)	
23	4392	CYSH2	T401-8			12-3-98	76.23	13.88	1.11
0.34	0.04	1.66	0.15	4.26	2.32	99.99	0.9430	MSH Set C, 41 ka	
24	3986	SKY-V-2	T364-5			5/97	76.34	13.98	1.19
0.28	0.03	1.62	0.13	4.22	2.21	100.00	0.9429	Skykomish Valley, WA	
25	1513	MOD-4 (2) (373)	T119-14			4/28/86	74.85	14.90	1.26
0.39	0.12	1.86	0.12	3.59	2.90	99.99	0.9426		
26	3073	ST HELENS Ye	T5-3			8/5/93	76.12	14.40	1.25
0.34	0.05	1.72	0.16	3.85	2.11	100.00	0.9422	MSH layer Ye 3.69 ka, cal.	
27	3774	942-209	major				77.12	14.59	1.48
0.39	0.06	1.87	0.13	2.71	1.65	100.00	0.9396		
28	429	Yn-7-15-72-8,	T3,4				75.54	14.23	1.40
0.37	0.08	1.81	0.15	4.27	2.14	99.99	0.9389		
29	3952	95T0-B260B	T360-2			4/97	76.72	13.48	1.18
0.31	0.05	1.59	0.14	3.83	2.70	100.00	0.9389		
30	4647	RAFT4673,	T405-10			04/01/00	75.14	14.46	1.35
0.38	0.04	1.92	0.14	4.22	2.35	100.00	0.9374		

31	4435	FL7.74-7.76M_POP1	T408-2			5-30-99	75.94	14.17	1.16
0.32	0.05	1.77	0.17	4.12	2.32	100.02	0.9365		
32	2958	RFUA-MFT-AV					76.85	13.32	1.21
0.37	0.00	1.60	0.15	4.00	2.50	100.00	0.9338		
33	3203	DJP-15-155.7	T302-4			3/25/94	76.10	14.41	1.04
0.32	0.07	1.47	0.13	3.88	2.59	100.01	0.9303		
34	4922	PLW8/11/01P1_POP1	T483-8			10-26-02	76.14	14.37	1.07
0.35	0.02	1.82	0.09	4.03	2.10	99.99	0.9285		
35	2955	RFUA-CHT-AV					76.29	13.53	1.37
0.39	0.00	1.58	0.13	4.34	2.38	100.01	0.9284		
36	3985	SKY-V-1	T364-4			5/97	76.40	13.91	1.17
0.29	0.04	1.65	0.15	4.13	2.27	100.01	0.9275		
37	3771	942-93					77.10	14.36	1.50
0.37	0.05	1.86	0.15	2.77	1.84	100.00	0.9271		

Glass geochemistry, sample TL100110-1

No.	Na2O	MgO	Al2O3	SiO2	K2O	CaO	TiO2	MnO	FeO	Total
266	2.6868	0.3674	13.3205	71.5057	1.9331	1.7199	0.0999	0.0283	0.9302	92.5918
267	2.6334	0.3187	13.2578	72.0018	1.9192	1.6739	0.1039	0.0516	0.9726	92.9329
269	2.8899	0.3341	13.4735	72.5853	1.9921	1.7041	0.1069	0.0211	0.9786	94.0856
270	2.8266	0.3507	13.5122	72.6141	1.9195	1.7862	0.1229	0.0366	1.0722	94.2410
272	2.7737	0.3314	13.3726	72.2150	1.9483	1.6750	0.1069	0.0355	1.0300	93.4884
273	2.8985	0.3238	13.4767	72.7344	1.9696	1.7029	0.1389	0.0244	1.0662	94.3354
275	2.8399	0.3089	13.1922	72.0748	1.9098	1.7101	0.1439	0.0411	1.0194	93.2401
278	2.9788	0.3179	13.5126	73.2177	1.8804	1.7448	0.1500	0.0544	0.9810	94.8376
279	2.9071	0.3317	13.4239	72.9951	2.0074	1.6850	0.1480	0.0422	1.0083	94.5487
281	2.5646	0.3532	13.3816	72.0120	1.9705	1.6913	0.1080	0.0256	1.0053	93.1121
283	2.7570	0.3180	13.1474	72.7394	1.9119	1.7014	0.1240	0.0300	0.9448	93.6739
284	2.8463	0.3175	13.3028	72.4911	1.9332	1.6014	0.1300	0.0494	0.9190	93.5907
Lo Total										
268	2.4632	0.2642	12.5422	69.6025	1.8975	1.6102	0.1219	0.0294	0.9877	89.5188
Feldspar										
282	6.3194	0.0170	26.6119	57.0214	0.2082	9.3277	0.0441	0.0399	0.2085	99.7981
Hi Fe										
280	4.6266	0.8236	15.5749	67.8329	2.0744	2.2639	0.7695	0.1372	3.4590	97.5620
274	2.6885	0.3604	12.9024	70.9455	3.2618	1.4788	0.4372	0.0643	1.7642	93.9031
277	3.7299	0.4090	14.0539	72.1950	2.6127	1.4875	0.4049	0.0986	1.6825	96.6740
285	2.4249	0.2217	12.2850	73.1364	3.8479	0.9843	0.3403	0.0194	1.5279	94.7878
Lo Ca										
276	2.4407	0.1731	11.0949	75.8200	2.6311	0.6695	0.1340	0.0722	0.8505	93.8860
271	2.1077	0.2473	12.6974	71.0111	1.9665	1.5061	0.1190	0.0144	0.7733	90.4428
Mean	2.8002	0.3311	13.3645	72.4322	1.9413	1.6997	0.1236	0.0367	0.9940	93.7232